Carbon 235 (2025) 120072

Contents lists available at ScienceDirect

Carbon

journal homepage: www.elsevier.com/locate/carbon

# High-temperature friction and oxidation resistance of self-sacrificial diamond-graphene heterostructures coatings

Shuyu Fan [a,b], Shu Xiao [a,*], Hu Zhang [a], Songsheng Lin [b,**], Jing Wu [a], Fenghua Su [a], Paul K. Chu [c]

[a] School of Mechanical & Automotive Engineering, South China University of Technology, Guangzhou, 510641, China
[b] Guangdong-Hong Kong Joint Laboratory of Modern Surface Engineering Technology, Guangdong Provincial Key Laboratory of Modern Surface Engineering Technology, Institute of New Materials, Guangdong Academy of Sciences, Guangzhou, 510651, China
[c] Department of Physics, Department of Materials Science and Engineering, and Department of Biomedical Engineering, City University of Hong Kong, Tat Chee Avenue, Kowloon, Hong Kong, China

ARTICLE INFO

*Keywords:*
Diamond
Graphene
Heterostructure
Friction
Oxidation
Self-sacrificial

ABSTRACT

The inherent brittleness and lack of self-support capabilities of diamond and graphene limit their application in durable lubrication systems. However, pre-encapsulating flexible graphene on diamond coatings holds immense potential to balance brittleness with toughness in high-temperature friction applications. Herein, diamond-graphene heterostructure coatings with a semi-coherent interface, characterized by robust bonding interspersed with dislocation defects, were synthesized *in situ* using hot-filament chemical vapor deposition. Benefiting from the synergistic effects of enhanced interfacial strength and oxygen-trapping capabilities, these coatings demonstrated over 35 % improvement in friction performance across various temperatures. Experimental and computational analyses indicated that the robust interface facilitates energy transfer, allowing graphene to undergo elastic adjustment and stress dissipation in a self-sacrificial manner before the brittle diamond experiences catastrophic failure. Additionally, the engineered defects within graphene layers serve as preferential adsorption sites for oxygen atoms, creating a high-energy barrier against oxygen diffusion into the diamond interior. These results reveal the influencing mechanisms of interfacial strength and defect engineering on diamond-graphene heterostructure coatings, setting the stage for next-generation materials tailored for high-temperature friction applications.

## 1. Introduction

Friction accounts for a significant portion of global energy consumption and contributes importantly to mechanical component failures, making lubrication a critical consideration in aerospace, wind energy, and automotive systems [1–4]. Solid lubricants with green-lubrication, high load-bearing and excellent chemical stability properties are increasingly favored in high-temperature applications over liquid or grease lubricants [5–7]. Carbon-based materials such as diamond, graphene, and carbon nanotubes exhibit excellent chemical stability, strength, thermal conductivity, and lubrication, making them promising candidates for solid lubricants [8–11]. While these materials individually have impressive attributes, their combination into composite systems may enhance mechanical properties and heat dissipation pathways due to their lattice compatibility [12,13]. Therefore, tailoring the synergistic interactions among carbon materials is essential for reliable performance in high-temperature friction application.

According to Archard's theory, solid lubricant composites should possess high strength and sufficient plastic deformability to reduce plastic deformation and frictional heating during wear [14]. This combination can prevent brittle fracture and strain softening to enhance the wear resistance. Notably, graphene with high toughness and flexibility can overcome the brittleness of diamond and subsequent fractures [15]. The high hardness, low surface activity, and minimal lattice mismatch of diamond make it ideal as a supporting layer for graphene [16,17]. Therefore, pre-encapsulating and flexibilizing graphene on diamond coatings presents significant potential to harmonize brittleness with toughness in high-performance friction applications [18]. Furthermore,

* Corresponding author.
** Corresponding author.
*E-mail addresses:* xiaos@scut.edu.cn (S. Xiao), linsongsheng@gdinm.com (S. Lin).

https://doi.org/10.1016/j.carbon.2025.120072
Received 19 September 2024; Received in revised form 23 December 2024; Accepted 30 January 2025
Available online 1 February 2025

the mechanical properties of both diamond and graphene are sensitive to temperature. Diamond dissipates heat by three-dimensional (3D) lattice vibrations, although its grain boundaries may increase the in-plane thermal resistance, leading to surface amorphization and thermal stress at a high temperature [19]. Graphene, a two-dimensional (2D) substance, has remarkable in-plane thermal conductivity but limited cross-plane heat transfer due to van der Waals forces, which restrict vertical heat dissipation [20]. Therefore, integrating graphene to address diamond lattice defects and leveraging diamond for vertical cooling channels is essential to establishing effective 2D-3D thermal conduction networks [21]. However, the detail mechanisms of diamond-graphene composites on friction and oxidation resistance at high-temperature application remain are still not fully understood.

Strategies to enhance mechanical properties of diamond-graphene composites include integrating individual carbon hybrid states into mixed $sp^2$-$sp^3$ amorphous carbon or directly forming heterostructures from two compatible carbon materials [22,23]. However, contrary to heterostructures, the disorder at amorphous carbon interfaces limits stable lubrication and thermal stability [24]. Currently, two types of heterostructures between diamond and graphene have been proposed: one involving a graphene-diamond diphase connected by weak van der Waals interactions, and the other featuring a covalently bonded interface with a reduced interlayer distance [25,26]. The construction of diamond-graphene heterostructures primarily through physical interactions such as π-π, van der Waals, and hydrophobic forces by transfer and assembly methods can significantly diminish their strength, hardness, and scratch resistance [27]. Conversely, heterostructures formed solely by covalent bonds may increase interfacial friction [28]. Therefore, developing a semi-coherent interface that balances van der Waals forces and covalent interactions is key to durable lubrication in diamond-graphene heterostructures. Efforts to achieve superlubricity under dry condition include forming graphene nanoscrolls with a nano-diamond core and leveraging micro-bearing rolling and incommensurate contact effects [29]. An important overlooked aspect is the impact of interfacial interactions between diamond and graphene on macroscale friction. Constructing a semi-coherent interface in diamond-graphene heterostructure coatings and elucidating the relationship between interfacial interaction and high-temperature friction and oxidation resistance mechanisms through experimental and atomic-scale theoretical models are thus essential.

Herein, we aim to regulate the interfacial interactions between diamond and graphene, promote the *in situ* growth of semi-coherent interfaces in diamond-graphene heterostructure coatings, and study the mechanisms responsible for the friction and oxidation resistance at various temperatures. Owing to practical application limitations of nanocrystalline diamond (NCD) coatings, which have fine grains and grain boundaries, compared to microcrystalline diamond (MCD) coatings, further optimization of its structure and properties is necessary [30]. Hence, diamond coatings with a nanocrystalline size are deposited by hot-filament chemical vapor deposition (HFCVD). The graphene coatings are precipitated *in situ* on the diamond surface by high-temperature annealing with nickel assistance. Molecular dynamics (MD) simulation is performed to examine the evolution of the mechanical strength and failure behavior in the diamond-graphene heterostructure with temperature and oxidation. First-principles calculations based on the density-functional theory (DFT) are also conducted to determine the effects of a self-sacrificial defective graphene layer on the oxygen atom adsorption energy, charge distribution, and diffusion energy barriers atop the diamond structure. The results provide fundamental information about the friction and oxidation resistance of diamond-graphene heterostructure coatings for high-temperature friction applications.

## 2. Experimental details

### 2.1. In-situ preparation of diamond-graphene heterostructure coatings

The schematic diagram of the *in situ* fabrication of diamond-graphene heterostructure coatings is shown in Fig. 1. Prior to deposition, the commercial WC-Co substrate (sourced from Zhuzhou Cementer Carbide Cutting Tools Co., Ltd.) was pre-treated by etching in the Murakami and acid solutions, and then seeded with the diamond powder suspension for 15 min ultrasonically [31]. In the HFCVD process (Carbon Competence, Austria) to form the diamond coating, the pressure was 0.003 mbar, and the filament and substrate temperatures were 2000 °C and 800 °C, respectively. A $CH_4$ (165 sccm) and $H_2$ (9000 sccm) gas mixture was then introduced to attain a working pressure of 5 mbar. After a duration of 6 h, the diamond coating with a nano-crystalline grain size was prepared.

Before graphenization, a Ni layer 70 nm thick was sputter-deposited on the NCD coatings using a Ni target (purity 99.99 %) in a magnetron sputtering direct current (DC) deposition system. Before starting the sputtering process, the vacuum chamber was evacuated to a base pressure of $1 \times 10^{-4}$ Pa to remove impurities. Argon gas (Ar, 99.99 % purity) was introduced to a working pressure of 0.3 Pa. Deposition was carried out using a DC current of 0.23 A and bias of −50 V for 5 min. Subsequently, the diamond-Ni coatings were annealed in a quartz tube at 1000 °C in the $Ar/H_2$ atmosphere for 10 min to produce graphenization without an additional carbon source. The residual Ni layers was etched chemically with an HCl and $HNO_3$ solution. The diamond-graphene heterostructure coatings were synthesized by the following steps [32]: (i) Bond breaking and rearrangement of carbon atoms in the diamond lattice, transitioning from $sp^3$ to $sp^2$ hybridization with the help of the Ni catalytic layer at a high temperature and $Ar/H_2$ atmosphere; (ii) Nucleation of small graphene domains extensively at the grain boundaries or defect regions of nanocrystalline diamond; (iii) Segregation and diffusion of carbon atoms, resulting in the merging and coverage of graphene domains across the entire diamond lattice during cooling.

### 2.2. Characterization and tribological tests

The surface morphology and elemental composition were observed by field-emission scanning electron microscopy (SEM, SU8220, equipped with energy-dispersive X-ray spectroscopy (EDS)). The microscopic morphology and fine structure were detected by scanning transmission electron microscope (STEM, Spectra 300) and electron energy-loss microscopy (EELS, GIF continuum 1065). The three-dimensional morphology and roughness were examined by atomic force microscopy (AFM, Dimension Edge). The surface contact angle was measured on the OCA40 tester. The phase composition was characterized by X-ray diffraction (XRD, Smartlab) using Cu-kα radiation. The chemical composition and wear tracks were measured by X-ray photoelectron spectroscopy (XPS, ESCALAB 250xi). The chemical functional groups were determined by Fourier transform infrared spectroscopy (FTIR, TENSOR27), and the peak representing diamond and graphene were examined by Raman scattering (LabRAM HR). The frictional performance at room temperature (25 °C, 50 % ± 5%RH) and high temperature (400 °C, 0–5%RH) was evaluated using a ball-on-disk tribometer (UMT-Tribolab, Bruker) with an $Al_2O_3$ counterpart ball (Φ6 mm, Ra = 12.7 nm). Three consecutive friction tests were executed, each using a rotation rate of 382 rpm (equivalent to 0.2 m/s) and a load of 1 N. These specific testing parameters were selected based on comprehensive literature review [33–36] and preliminary tribological experiments conducted under different operating conditions (Fig. S1). The wear track and wear volume were obtained by 3D profilometry (Dektak XT). The wear rates were derived by the Archard equation $W = V/(F \times S)$, where $V$ denotes wear volume, $F$ is the sliding distance, and $S$ stands for the applied load.

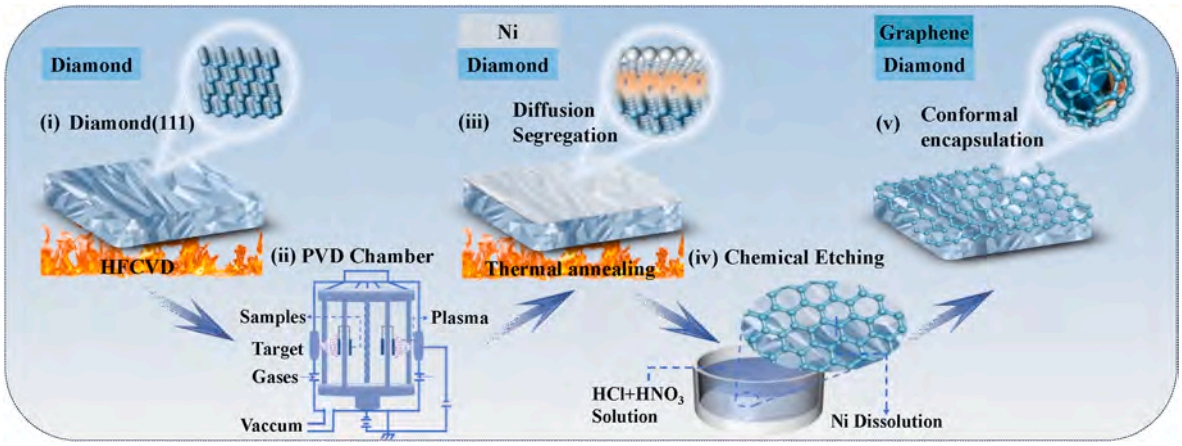


**Fig. 1.** Schematic diagram illustrating the fabrication process of diamond-graphene heterostructure coatings: (i) diamond deposition by HFCVD method, (ii) Ni catalyst layer deposition on diamond surface by PVD technology, (iii) carbon diffusion and segregation through thermal annealing, (iv) Ni removal by chemical etching, and (v) conformal graphene growth on diamond surface. (A colour version of this figure can be viewed online.)

### 2.3. Molecular dynamics calculations

To investigate the mechanical adhesion strength and failure mechanisms of diamond and diamond-graphene heterostructures at different temperatures, molecular dynamics simulation was performed on a large-scale atomic/molecular massively parallel simulator (LAMMPS) in conjunction with reactive force-field (ReaxFF) [37,38]. The total energy and forces on each atom in the ReaxFF are listed in Equation (1):

$$E_{total} = E_{bond} + E_{over} + E_{under} + E_{lp} + E_{val} + E_{tors} + E_{vdWaals} + E_{Coulomb} + E_{trip}, \quad (1)$$

where $E_{bond}$, $E_{over}$, $E_{under}$, $E_{lp}$, $E_{val}$, $E_{tors}$, $E_{vdWaals}$, $E_{Coulomb}$, and $E_{trip}$ represent the bond energy, over-coordination energy penalty, under-coordination stability, lone-pair energy, valence angle energy, torsion angle energy, van der Waals energy, Coulomb energy, and triple bond stabilization energies, respectively.

To take into account the robust interface observed between diamond and graphene in experimental characterizations, system was constructed for both the diamond (111) structure and a diamond (111)-graphene heterostructure featuring four stacked graphene layers interconnected through hexagonal rings (Fig. S2). The initial system was developed in three steps. The diamond bulk was first optimized using Materials Studio software and cleaved along the C (111) surface, which represents the most energetically favorable exposed surface. Subsequently, a four-layer graphene structure was constructed and optimized, then connected to the diamond surface through hexagonal rings, resulting in a diamond-to-graphene atomic ratio of 58.3 %–41.7 %. Finally, the initial system was configured with dimensions of 42 Å along the *x*-axis, 12 Å along the *y*-axis, and 11 Å along the *z*-axis, and exported to a LAMMPS compatible format. To investigate the effects of oxidation on the mechanical properties and multiple interfacial interaction of both diamond and diamond-graphene structures, 10 oxygen atoms were introduced into a stretching model to more accurately simulate realistic oxidation processes. Before conducting uniaxial tensile simulations at various temperatures using a Berendsen thermostat, the temperature was raised to either 300 K or 600 K for a period of 2.5 ps and then maintained for 1.25 ps to ensure system temperature stability at the set value. The basic stability of the system was confirmed through analysis of energy and temperature evolution curves during both the heating and temperature maintenance stages (Fig. S3). The micro-canonical ensemble (NVE) was adopted to further stabilize the system at temperatures of 300 K or 600 K. Subsequently, the system was equilibrated along the *x*-direction to alleviate internal stress and stabilize atomic positions. In the stretching process, uniaxial stretching was performed along the *x*-axis direction using a 0.05 % uniaxial strain rate for 4, 000 steps under NVE ensemble. The simulation employed periodic boundaries in the *x*- and *y*-directions, a flexible boundary in the *z*-direction, and a time step of 0.25 fs.

### 2.4. First-principles calculations

Density-functional semi-core pseudopotential (DSPP) methods were executed using the DMol3 package during the first-principles calculations (DFT) [39]. The system construction commenced with the optimization of bulk diamond, followed by the cleavage of an eight-layer diamond (111) surface. A diamond (111) slab containing three defect sites was subsequently created with dimensions of 7.58 Å × 7.58 Å × 30 Å to align with experimentally observed structures (Fig. S4a). Based on experimental observations indicating that partially defective graphene layers align parallel to diamond surfaces, a heterostructure was formed by placing a graphene layer with a single defect atop the optimized diamond (111) slab. The resulting diamond-graphene heterostructure measured 7.49 Å × 7.49 Å × 22 Å and exhibited a lattice mismatch of less than 5 % (Fig. S4b), consistent with experimental findings in this work. The atomic composition of the heterostructure comprised approximately 80 % diamond atoms and 20 % graphene atoms. A vacuum layer thicker than 10 Å was incorporated to prevent interactions between periodic images. The exchange-correlation energy was described using the Perdew-Burke-Ernzerhof (PBE) functional within the generalized gradient approximation (GGA), with dispersion corrections implemented through Grimme's second-generation empirical correction term (DFT-D2) [40–42]. Spin polarization was incorporated in the calculations. A global orbital cutoff radius of 3.7 Å was defined to fully account for the atomic interactions. A 2 × 2 × 1 *k*-point grid was used to ensure accuracy, and charge compensation was applied to the relevant structures. The optimization procedure was carried out until satisfy convergence criteria with the self-consistent field (SCF) convergence tolerance, total energy, atomic forces, and maximum displacement set at less than $2.7 \times 10^{-5}$ eV, $2.7 \times 10^{-4}$ eV/atom, 0.05 eV/Å, and $5 \times 10^{-3}$ Å, respectively. Structural characterizations revealed chemically active defect site in both diamond and diamond-graphene structures, which serve as preferential oxygen adsorption site. Therefore, single-oxygen models with stable adsorption configurations above the defective structural surfaces with C atomic vacancy were developed to investigate oxygen-carbon interactions at specific oxidation site. Further investigations were conducted to elucidate how oxygen atoms influence the adsorption energy, charge density, orbital interactions, diffusion paths, and diffusion barriers of defective diamond and defective diamond-graphene structures. The energy barrier and minimum energy path for the diffusion of oxygen atoms were determined using the linear/quadratic synchronous transit (LST/QST) method [43]. The

adsorption energy ($E_{ads}$) was utilized to assess the stability of the adsorption structure, with negative values indicating a more stable state. The adsorption energy was calculated by Equation (2) [44]:

$$E_{ads} = E_{total} - E_O - E_{surface}, \quad (2)$$

where $E_{total}$ represents the total energy of the adsorption system, $E_O$ represents the energy of isolated O atom, $E_{surface}$ represents the energy of the surface. Additionally, Mulliken population analysis was conducted to quantify the charge distribution between the oxygen atom and its adjacent carbon atom [45,46]. This method allows for a qualitative assessment of bond strength, where a higher Mulliken population reflects a stronger bond interaction, while a lower population indicates a weaker interaction between atoms [47]. The diffusion energy barrier ($\Delta E_{barrier}$) was used to assess the ease of oxygen atom diffusion, with a high value of $\Delta E_{barrier}$ representing better oxidation resistance. $\Delta E_{barrier}$ was calculated using Equation (3) [48]:

$$\Delta E_{barrier} = E_{TS} - E_{initial}, \quad (3)$$

where $E_{initial}$ and $E_{TS}$ are the energy of the initial state and the energy of the transition state, respectively.

## 3. Results and discussion

### 3.1. Microstructures of diamond-graphene heterostructure coatings

Detailed STEM observations of the diamond-graphene heterostructure coatings reveal the atomic-resolution structures of diamond and graphene, along with the interfaces between them (Fig. 2). As shown in Fig. 2a, the diamond crystals are uniformly covered by graphene domains, showing a spontaneously *in situ* grown conformal coating. The uniform and stable graphene coating on the diamond surface is formed by minimizing the surface energy, reducing lattice mismatch, and leveraging the inherent compatibility of carbon structures [49]. To examine the changes in carbon bonding configurations in the entire diamond-graphene heterostructure, a linear EELS scan with high spatial resolution is conducted (Fig. 2b). The peak at approximately 285 eV is attributed to the carbon 1s to π* transition characteristic of graphene carbon, whereas the peak at about 292.6 eV is associated with the carbon 1s to σ* transition indicative of diamond carbon [50,51].

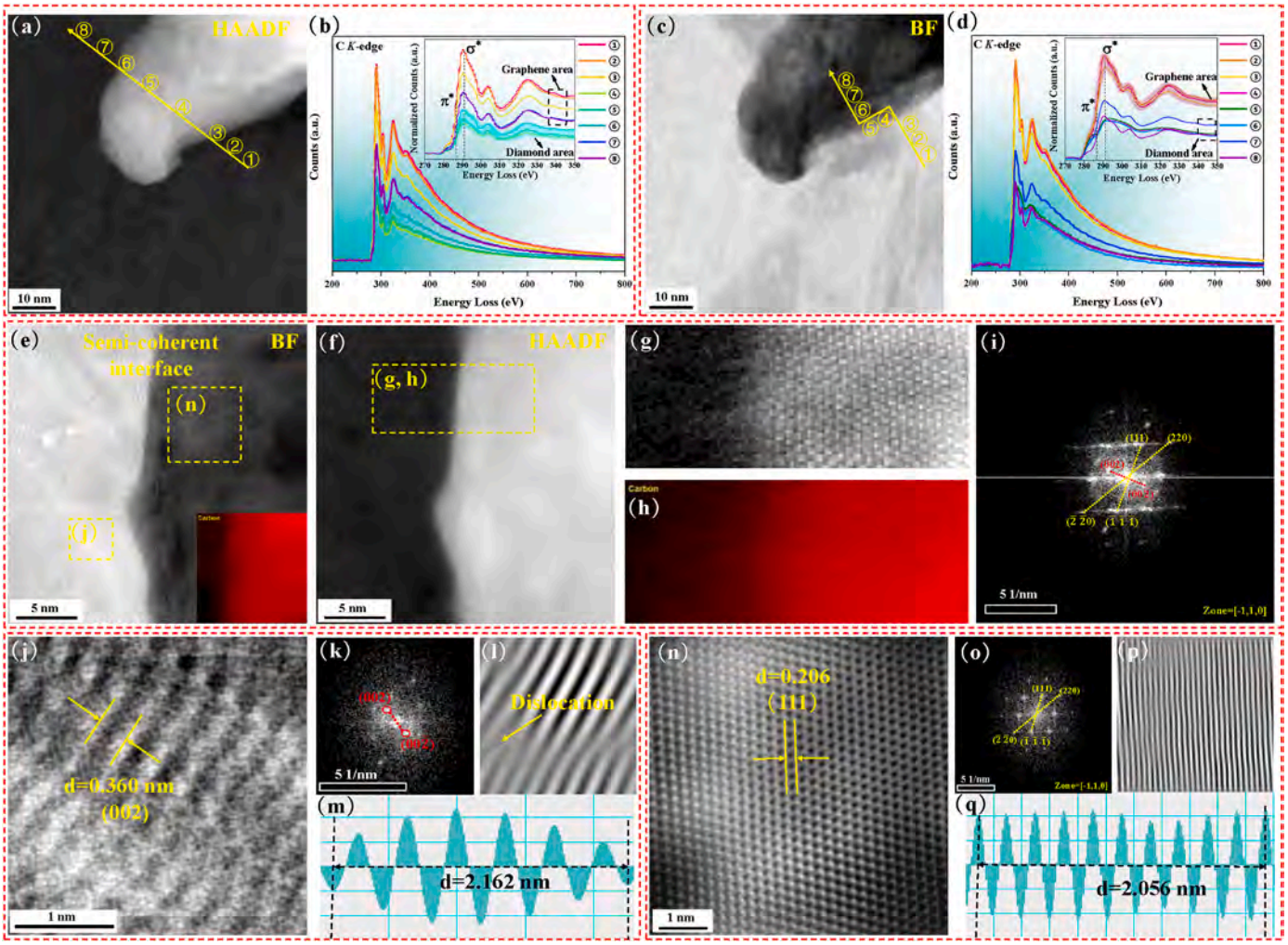


**Fig. 2.** STEM characterization of the diamond-graphene heterostructure coatings: (a) HAADF-STEM image of the as-grown graphene on diamond; (b) EELS analysis along the trajectory marked by yellow dashed line in (a), points 1–8, with inset showing magnified spectra in 270–350 eV energy loss region; (c) BF-STEM image of the as-grown graphene on diamond; (d) Localized EELS analysis along the yellow dashed line in (c), points 1–8, with inset showing magnified spectra in 270–350 eV energy loss region; (e) BF-STEM image of the interface with an inset showing carbon elemental mapping; (f) HAADF-STEM image at the interface; (g, h) HAADF-STEM image highlighting the EELS mapping area shown in (f); (i) Selected area electron diffraction (SAED) pattern form the interface shown in (e); (j–m) Magnified views (BF-STEM, SAED, local inverse fast Fourier transform (IFFT), and interlayer spacing) of graphene area, as marked yellow rectangular dashed areas (j) in (e); (n–q) Magnified views (BF-STEM, SAED, local IFFT, and interlayer spacing) of the diamond area, as marked yellow rectangular dashed areas (n) in (e). (For interpretation of the references to color in this figure legend, the reader is referred to the Web version of this article.)

Traversing from graphene through diamond and returning to graphene domain (specifically, points 1 to 8 in Fig. 2a), there is an obvious reduction in the intensity of the σ* and π* peaks in the diamond domain. This indicates the coexistence of both graphene-and diamond carbon in the heterostructure, corresponding to the high-angle annular dark field (HAADF) imaging observation. To further explore the evolution of the interface structure, localized linear EELS scanning is carried out at the diamond-graphene interface. The results show a decline in the intensities of the σ and π peaks from the graphene region to the diamond region, specifically from points 1 to 8 (Fig. 2c–d). Notably, the σ* and π* peak intensities observed at EELS points 4 to 6 in the interfacial region exhibit intermediate values between those typical of diamond and graphene, indicating the coexistence of a graphene and diamond bonded state at the interface (Fig. 2d). Moreover, the robustly bonded interface shows an enhanced interfacial adhesion and creates a continuous energy transfer pathway, subsequently facilitating efficient thermal and mechanical energy transfer between the diamond and graphene structure, as reported by Yan et al. [52].

Fig. 2(e–g) depict the bright field (BF-STEM) and HAADF-STEM images, where a semi-coherent interface between diamond and graphene is observed. This is characterized by some regions maintaining good lattice matching in addition to the partial presence of dislocations at the interface, likely due to the lattice mismatch between diamond and graphene ranges from 1 % to 10 % [53]. EELS elemental mapping confirms the carbon distribution across the interface, as illustrated in the inserts in Fig. 2e and h). The crystalline nature of graphene (002) and diamond (111) along the [−110] axis is exhibited in Fig. 2i. To perform a detailed examination of crystalline features and lattice mismatch between graphene and diamond, the magnified images of the yellow rectangular dashed areas labeled (j) and (n) in Fig. 2e are presented in Fig. 2j and n, respectively. The *d*-spacings of 0.360 nm and 0.206 nm are consistent with the graphene (002) plane (Fig. 2k–m) and diamond (111) plane (Fig. 2o–q), respectively, indicating a lattice mismatch of about 4 % at the interface (Fig. 2j–q) [54]. The increased *d*-spacings of graphene, exceeding the theoretical value of 0.340 nm, suggests that the graphene layer parallel to the diamond surface is in an expanded state due to dislocations, as shown in Fig. 2l. The appropriate lattice mismatch introduces elastic strain energy, aiding stress relief through dislocation movement and improving structural stability. Moreover, the partial dislocation sites serve as favorable preferential adsorption sites and are expected to trap oxygen atoms by forming stable oxygen-containing bonds [55,56], thereby potentially hindering oxygen diffusion and increasing the diffusion barrier. This is supported by the subsequent XPS measurements showing abundant C–*O*–C bonds on diamond-graphene heterostructure surfaces and DFT calculations indicating higher adsorption energies and diffusion barriers. Therefore, the diamond-graphene heterostructure with semi-coherent interface has enhanced mechanical and oxidation resistance properties, similar to the results obtained by Németh et al. [57]. More importantly, the semi-coherent interface allows for easy shear sliding through incommensurate contact, which is essential to enhanced friction performance.

### 3.2. Morphology of diamond and diamond-graphene heterostructure coatings

To study the variations in surface morphology, roughness and wettability among the diamond coating and diamond-graphene heterostructure coatings, SEM, high-resolution TEM (HR-TEM), AFM, and contact angle measurements are carried out (Fig. 3). The surface morphology of the diamond coating shows a cauliflower-like structure, with grain sizes ranging from 1 to 100 nm, consistent with the characteristics of nanocrystalline diamond (Fig. 3a). Grain boundaries on the diamond surface are distinctly observable, with HR-TEM revealing symmetrically arranged twin crystals within these boundaries (Fig. 3b). Due to the lattice discontinuity at twin boundaries, the transmission paths for stress and heat may be disrupted, potentially resulting in increased localized thermal stress [58]. The graphene overlayer exhibits dense growth with a cauliflower morphology, conformally adhering to the rugged surface of underlying nanocrystalline diamond coating, as shown in Fig. 3e. Considering that nanocrystalline diamond has a polycrystalline structure, the conformal encapsulation of the graphene layer indicates uniform *in situ* growth on various diamond crystal facets. The growth process and morphology of the diamond-graphene heterostructure coating is closely related to the crystal structure of the

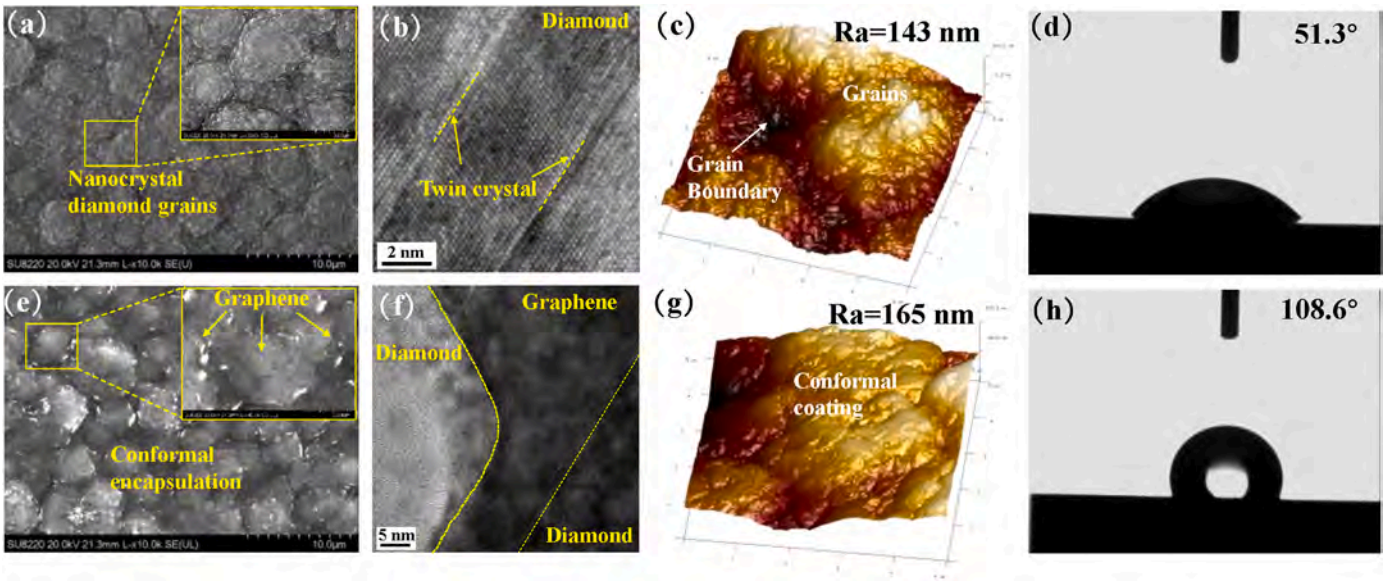


**Fig. 3.** Morphological, microstructure, topographical, and wettability characterization of the diamond and diamond-graphene heterostructure coatings: (a) SEM surface morphology of diamond coating, with an inset showing a higher magnification view of a localized area; (b) HR-TEM image of the grain boundary; (c) AFM 3D topographic image (5 μm × 5 μm) of diamond coating; (d) Photographs showing the contact angles on the diamond coating; (e) SEM surface morphology of diamond-graphene heterostructure coating, with an inset showing a higher magnification view of a localized area; (f) HR-TEM microstructure of the interface between diamond and graphene; (g) AFM 3D topographic image (5 μm × 5 μm) of diamond-graphene heterostructure coating; (h) Photographs showing the contact angles on diamond-graphene heterostructure coating. (A colour version of this figure can be viewed online.)

underlying diamond. Specifically, nanocrystalline diamond coatings, characterized by fine grains and numerous grain boundaries, serve as preferred nucleation sites for small graphene domains. The grain boundaries enhance lateral diffusion and realignment of carbon atoms under high temperature and subsequent cooling conditions and promote the uniform graphene coverage through the strong affinity of $sp^2$ lattice self-assembly. The diamond-graphene interface, clearly separated by the dashed line marked in the HR-TEM image (Fig. 3f), shows graphene parallelly arranged on top of the diamond and laterally connected through a robust bonded heterostructure, in line with the STEM results. These interfacial structures play distinct roles in enhancing the adhesion strength, and they provide experimental evidence for the construction of subsequent theoretical models.

The AFM images (5 μm × 5 μm) show a rougher surface morphology and roughness of diamond-graphene heterostructure coatings compared to diamond coatings, corroborating the SEM results. The roughness values of the diamond and diamond-graphene heterostructure coatings are 143 nm and 165 nm, respectively (Fig. 3c and g), indicating a direct relationship with the conformal encapsulation of the graphene layer on diamond coating during *in situ* growth. The graphene layer develops a rough and densely structured surface topography by overlaying the grain boundaries, crystallites, and defect edges of the diamond. A significant difference in contact angles is observed between diamond and the diamond-graphene heterostructure coating, with the values of 51.3° and 108.6°, respectively (Fig. 3d and h). This indicates the graphene layer further reduces the diamond surface energy, resulting in a more hydrophobic surface compared to the diamond coating alone, attributable to the roughened surface and altered chemical properties [59,60]. Specifically, the rough surface structures create air gaps, effectively reducing the actual contact area between the surface and liquid. This reduction in contact area increases the contact angle and enhances the surface hydrophobic properties. Furthermore, the parallel arrangement of graphene on diamond produces preferred adsorption sites for oxygen atoms, leading to the formation of a stable layer of graphene oxide with reduced surface energy. The smaller contact area and surface energy of the diamond-graphene heterostructure coating enhance the hydrophobic properties for better wear and oxidation resistance.

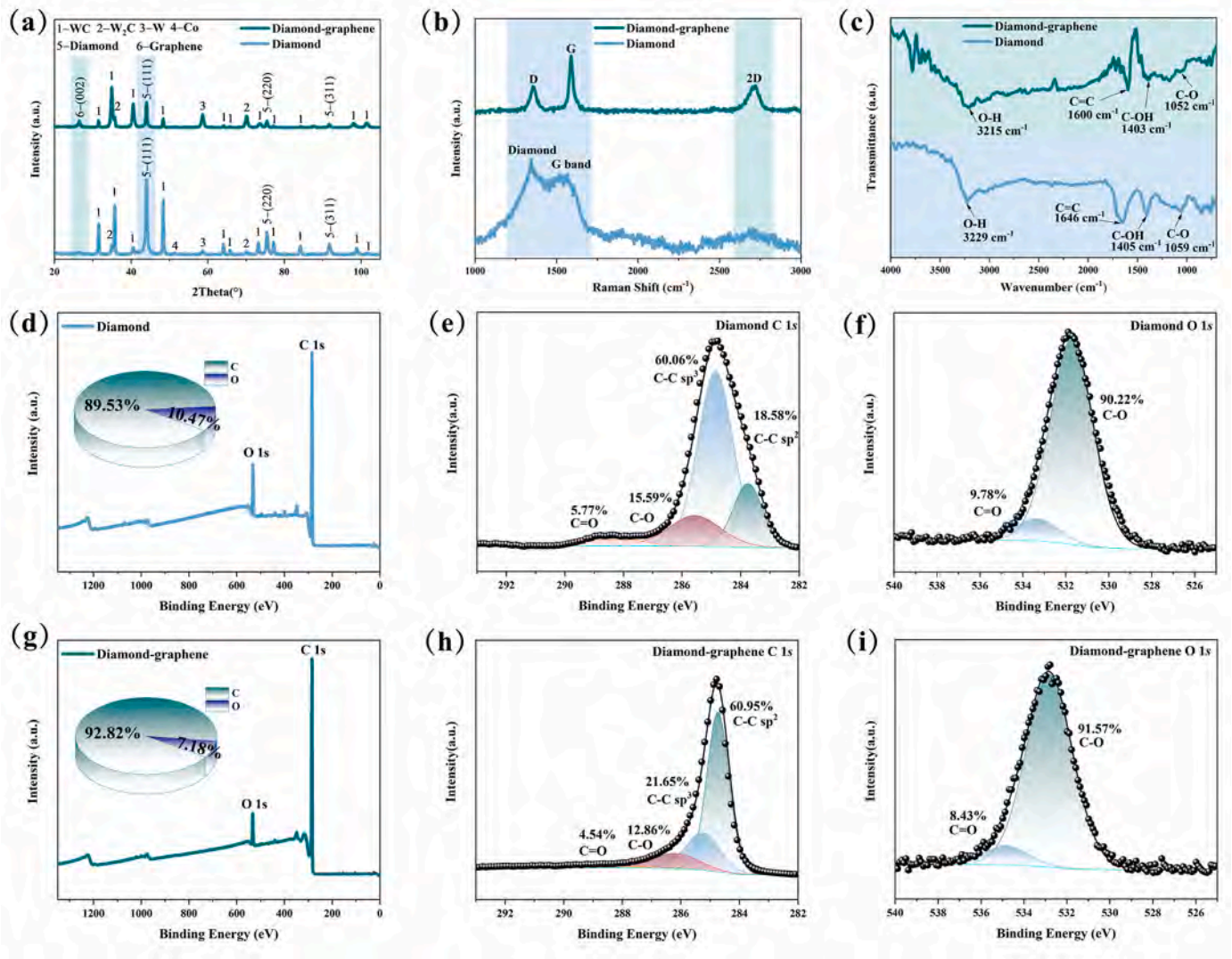


**Fig. 4.** Structural characterization of the diamond and diamond-graphene heterostructure coatings: (a) XRD patterns, (b) Raman scattering spectra, and (c) FTIR spectra, where blue and green curves represent diamond and diamond-graphene heterostructure coatings, respectively; (d) XPS survey spectra of the diamond coating; High-resolution XPS spectra with Gaussian fit of (e) C 1*s* and (f) O 1*s* spectra of the diamond coatings; (g) XPS survey spectrum of the diamond-graphene heterostructure coating; High-resolution XPS spectra with Gaussian fit of (h) C 1*s* and (i) O 1*s* in the diamond-graphene heterostructure coatings. (For interpretation of the references to color in this figure legend, the reader is referred to the Web version of this article.)

### 3.3. Structure of diamond and diamond-graphene heterostructure coatings

The microstructure and chemical properties of the prepared diamond and diamond-graphene heterostructure coatings are shown in Fig. 4. The three main diffraction peaks around 43.98°, 75.57°, and 91.71° can be assigned to the (111), (220), and (311) in diamond coatings, and the strong and sharp peak demonstrates excellent crystallinity (Fig. 4a). The preferential orientation of diamond (111) is conducive to promoting the growth of low-stress and high-quality graphene due to the minimal lattice mismatch with graphene [61]. After graphenization, the main diffraction peaks align with those previously identified in diamond, with the exception of the (002) peak at 26.55°, which is characteristic of graphene. Moreover, the reduction in diamond characteristic peaks, coupled with the enhancement of graphene characteristic peaks in the diamond-graphene heterostructure coatings, indicates an increase in the graphene content in the composite.

Raman scattering is performed to study the surface quality and residual stress of graphene and diamond coatings (Fig. 4b). The residual stress in the diamond coating is calculated as $\sigma = -0.567\ (v_m\text{-}v_0)$ (GPa), with $v_m$ at 1337 $cm^{-1}$ for the diamond peak and $v_0$ at 1332 $cm^{-1}$ for natural diamond. This results in a compressive stress of −2.835 GPa due to difference in thermal expansion coefficients and grain boundary extrusion during growth [62]. Furthermore, the weak and broad G peak at 1563 $cm^{-1}$ corresponding to the $sp^2$ carbon vibration at the grain boundaries, consistent with the SEM and HR-TEM results. In the diamond-graphene coatings, the dominant D peak at 1357 $cm^{-1}$, G peak at 1589 $cm^{-1}$, and 2D peak at 2712 $cm^{-1}$ are characteristic of graphene, with the absence of diamond signals indicating complete graphene coverage on diamond coating [63]. The $I_D/I_G$ and $I_{2D}/I_G$ ratios serve as quantitative measures of the defect density and graphene coverage as well as the number of layers, respectively [64]. The presence of defective and multilayer graphene on the diamond surface is evidenced by an $I_D/I_G$ ratio of 0.65 and an $I_{2D}/I_G$ ratio of 1.18, respectively. The increased defects and layers in graphene arise from the uneven topographies and grain boundaries of diamond coatings, where cauliflower-like features on the diamond surface act as nucleation sites that lead to dislocations and folds in graphene during growth.

To assess the correlation between chemical functional groups and wettability and oxidation resistance of diamond and diamond-graphene heterostructure coatings, FTIR and XPS are performed. As shown in Fig. 4c, the peak at 1600~1646 $cm^{-1}$ corresponds to the stretching vibration of the $sp^2$ hybridized carbon, characteristic of the C═C groups in the hexagonal aromatic ring found in graphene and at the grain boundaries of diamond coating [65]. Additional peaks corresponding to C–O (1052~1059 $cm^{-1}$), C–OH (1403~1405 $cm^{-1}$), and O–H (3215~3229 $cm^{-1}$) indicate the influence of intermolecular carbon-oxygen bonding interaction and water molecules adsorption [66]. The diamond-graphene heterostructure coatings exhibit a diminished absorption curve compared to pure diamond coatings, reflecting a mitigated exposure of diamond surface functional groups due to the present of graphene. This is supported by the observed weaker peaks, likely a result of water desorption and correlating with enhanced hydrophobicity as demonstrated by wettability results. Furthermore, the trend of diminishing oxygen-containing groups stemming from the incorporation of graphene indicates an attenuation of oxidative reactions. The integration of graphene into diamond decreases the surface energy and bolsters the oxidation resistance, potentially improving the high-temperature oxidation and friction resistance characteristics.

Fig. 4d–i shows the C 1*s* and O 1*s* XPS spectra for diamond and diamond-graphene heterostructure coatings at binding energies of 284.5 eV and 531.0 eV, respectively [67,68]. The spectra indicate a lower degree of oxidation in the diamond-graphene heterostructure coating, with O 1*s* accounting for 7.18 % (Fig. 4g) compared to 10.47 % in the pure diamond coatings (Fig. 4d), in line with FTIR results. As shown in Fig. 4e, the C 1*s* spectra from the diamond surfaces is deconvoluted into four components, including C–C $sp^3$ (284.9 eV, 60.06 %), C–C $sp^2$ (283.8 eV, 18.58 %), C–*O*–C (285.6 eV, 15.95 %), and C═O (288.6 eV, 5.77 %). The C–C $sp^3$ peak is the most prominent on the diamond surface, whereas C–C $sp^2$ is primarily associated with the grain boundaries. In the diamond-graphene heterostructure coating, the C–C $sp^2$ content increased to 60.95 % and the C–C $sp^3$ content decreased to 21.65 %, confirming the coverage of graphene on the diamond coatings (Fig. 4h). The reductions of 4.54 % for C═O suggest the protective role of graphene in reducing oxidation. Fig. 4f and i exhibit two principal peaks in the O 1*s* spectra for C–*O*–C (531.7 eV, 90.22 %) and C═O (533.7 eV, 9.78 %) in the diamond coating, compared to C–*O*–C (532.8 eV, 91.57 %) and C═O (534.9 eV, 8.47 %) in the diamond-graphene coatings. The increased C–*O*–C content in the diamond-graphene heterostructure coating suggests the formation of stable surface epoxy groups, which inhibit interior oxidation. Conversely, more C═O groups on the diamond coating boost the reactivity but lower the stability, potentially reducing the resistance to oxidation and wear.

### 3.4. Tribological properties and mechanisms of diamond and diamond-graphene heterostructure coatings at various temperatures

Ball-on-disk dry friction experiments are performed at different temperatures on the diamond and diamond-graphene heterostructure coatings. Fig. 5a presents the coefficient of friction (COF) curves of both coatings versus sliding time at room temperature (RT) and 400 °C together with the average COFs. The friction properties of diamond and diamond-graphene coatings differ obviously between RT and 400 °C. At RT, the friction curve shows the typical three-phase wear process manifested by an initial increase due to microscopic surface irregularities during the running-in phase, a gradual decrease as a lubrication film forms in the transitional phase to reduce direct contact, and stabilization in the steady-state phase as the friction interfaces become dynamically smooth [69]. In contrast, at a high temperature, the friction curve rises and then stabilizes without a noticeable decrease. During the running-in phase, the friction coefficients increase continuously due to accelerated chemical reactions such as softening and oxidation. The steady-state phase is characterized by the formation of a stable oxide layer, leading to a relatively stable friction coefficient. The data show that the average COF for diamond and diamond-graphene heterostructure coatings increases progressively with temperature, a trend also reported for other materials susceptible to high-temperature wear [70–72]. Notably, the COF curves measurements demonstrate a unique temperature-dependent trend. Both coatings show initially reduced friction at elevated temperatures compared to room temperature, followed by a progressive increase that eventually surpasses room-temperature values. The initial lower friction at elevated temperatures can be attributed to enhanced thermal activation effects promoting lubricating film formation and more efficient heat dissipation through the materials' high thermal conductivity [73,74]. However, prolonged high-temperature exposure leads to increased friction through accelerated humidity reduction, surface oxidation, mechanochemical degradation, and thermal expansion mismatch-induced structural deterioration [75]. Compared to diamond coatings, diamond-graphene heterostructure coatings consistently exhibit a significantly lower average COF at both room temperature and 400 °C. The enhanced lubrication is attributed to graphene's layered structure and high in-plane thermal conductivity, which facilitates interlayer sliding and heat dissipation, respectively.

Fig. 5b presents the 3D profiles, line scans, and wear rates of diamond and diamond-graphene heterostructure coatings at RT and 400 °C. Hardly any severe wear is observed from the coatings, and the wear tracks are evenl elevated above the surrounding surface. This phenomenon can be attributed to the exceptional hardness and high wear resistance of diamond relative to softer $Al_2O_3$ counter-balls. During contact, the diamond coatings can better resist deformation, resulting in greater materials removal from $Al_2O_3$, which then tends to accumulate

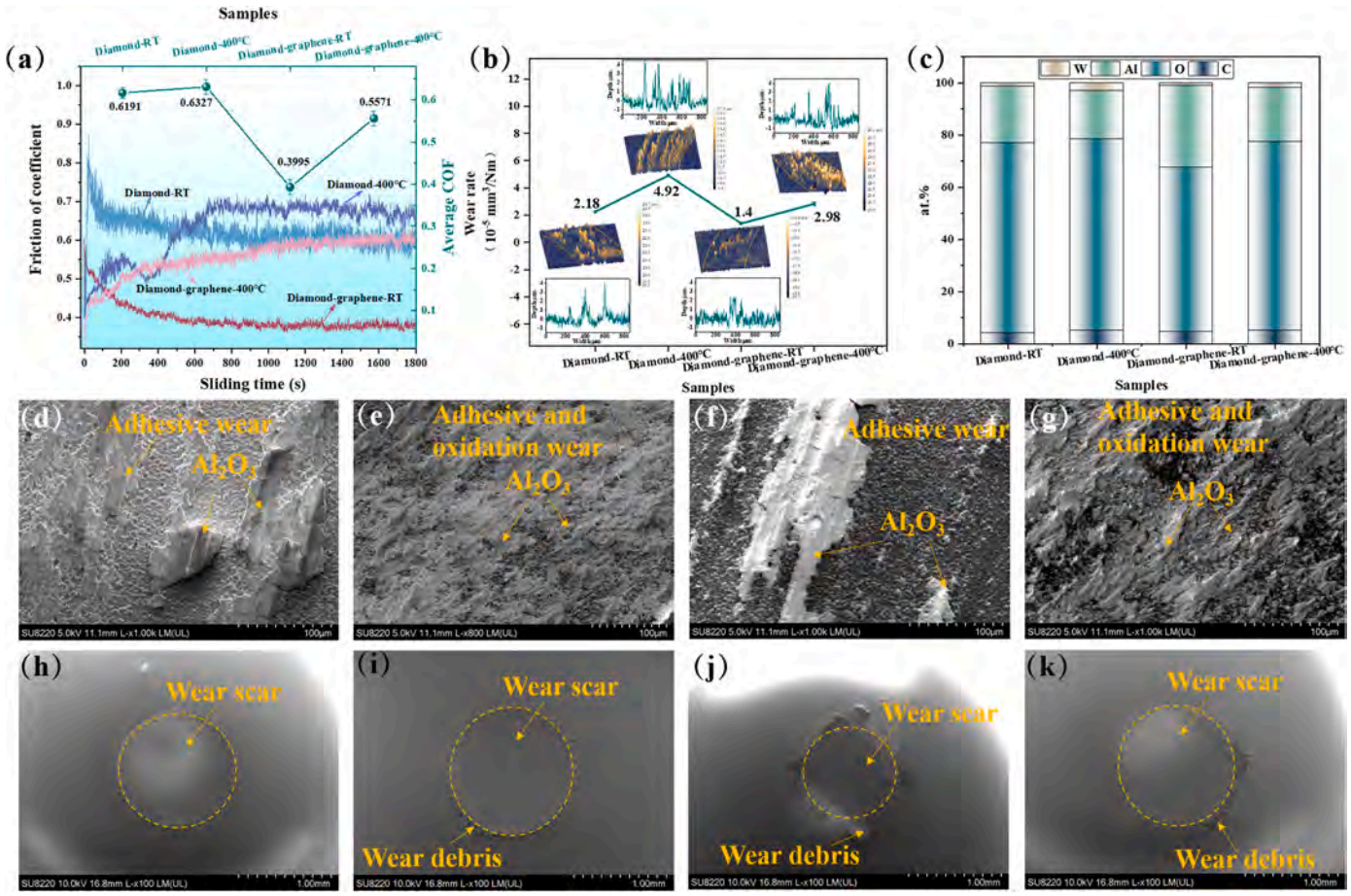


**Fig. 5.** Tribological properties of the diamond and diamond-graphene heterostructure coatings: (a) Coefficients of friction versus sliding time and average coefficient of fiction; (b) Three-dimension morphology mappings, line scans, and wear rates of the wear track (c) Chemical composition of wear tracks at various temperatures; Surface morphology of the wear tracks after friction for (d) diamond coating at RT, (e) diamond coating at 400 °C, (f) diamond-graphene heterostructure coating at RT, and (g) diamond-graphene heterostructure coating at 400 °C; Surface morphology of the wear scars on the counter-balls for (h) diamond coating at RT, (i) diamond coating at 400 °C, (j) diamond-graphene heterostructure coating at RT, and (k)diamond-graphene heterostructure coating at 400 °C. (A colour version of this figure can be viewed online.)

and adhere to the harder surfaces to form elevated tracks. Consequently, the wear rates for the $Al_2O_3$ counter-balls of the diamond coating are $2.18 \times 10^{-5}$ mm$^3$/Nm at RT and $4.92 \times 10^{-5}$ mm$^3$/Nm at 400 °C. In the diamond-graphene heterostructure coating, the wear rates for the $Al_2O_3$ counter-balls are $1.4 \times 10^{-5}$ mm$^3$/Nm at room temperature and $2.98 \times 10^{-5}$ mm$^3$/Nm at high temperature. The enhanced wear at elevated temperatures can be primarily attributed to the rapid moisture evaporation, reducing surface humidity to approximately 0%RH. This phenomenon eliminates both the lubricating effect of water-based tribochemical films and the surface passivation of dangling bonds [76, 77]. Additionally, the high-temperature environment promotes thermal oxidation and structural degradation, resulting in increased solid-solid contact and accelerated wear [78]. This indicates that the diamond-graphene heterostructure coating enhances the wear resistance and reduces the wear rate by over 35 % compared to diamond coatings at both room and high temperatures. Furthermore, a higher concentration of oxygen is observed from the wear track of the diamond coatings compared to diamond-graphene heterostructure coatings (Fig. 5c), implying that the diamond surfaces undergo more severe oxidation wear under thermal stress, underscoring the superior oxidation resistance of diamond-graphene coatings under similar conditions. As shown in Fig. 5d–g, the SEM images of the wear tracks reveal that after friction at RT and 400 °C, some $Al_2O_3$ debris adheres to the surface of the coatings, consistent with the 3D profiles. At a high temperature, the $Al_2O_3$ undergoes thermal softening and deformation, facilitating more uniform and flattened adhesion to the coating surfaces. Additionally, the wear tracks on the diamond-graphene heterostructure coatings (Fig. 5d–e) exhibit reduced adhesion and oxidative wear in comparison to those on diamond coatings (Fig. 5f–g) at both temperatures. Fig. 5h–k shows the SEM images of the wear scars on the counter-balls, revealing significant scratches and deep furrows indicative of severe adhesive wear during sliding. The counter-balls interacting with the diamond-graphene heterostructure coatings show smaller wear scars, even at high temperatures (Fig. 5j–k). This demonstrates the combined benefits of mechanical strength, lubrication properties, and oxidation resistance, which contribute to the superior friction performance of the diamond-graphene heterostructure coatings at various temperatures.

To further study the lubrication and tribochemical mechanism of diamond and diamond-graphene coating, Raman scattering and XPS are performed on the wear tracks. As shown in Fig. 6a–b, the wear-induced leftward shift of the diamond peak and enhanced G peak relative to their pre-wear states indicate an increase in residual tensile stress and structural disorder in the diamond coating during the friction test at both RT and 400 °C. The shift from residual compressive stress to residual tensile stress arises from stress relaxation and redistribution triggered by the friction process. Specifically, at 400 °C, the residual stresses in the wear track center and edge are 4.536 GPa and 3.969 GPa, respectively, surpassing those at RT of 3.402 GPa at the center and 2.835 GPa at the edge (Table 1). This elevation in residual stress at high temperatures stems

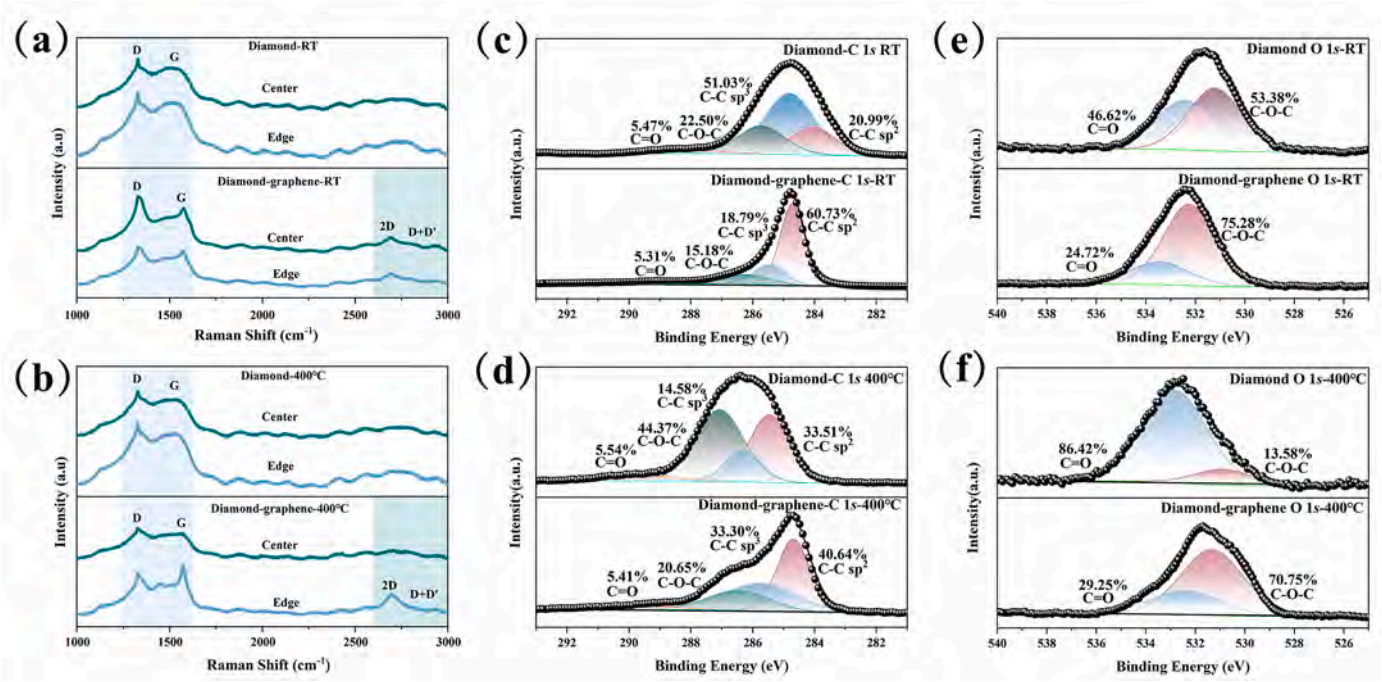


**Fig. 6.** Structural characterization of wear tracks on diamond and diamond-graphene heterostructure coatings: (a) Raman scattering spectra of the center and edge of the wear track after friction at RT; (b) Raman scattering spectra of the center and edge of the wear track after friction at 400 °C; (c) High-resolution XPS spectra of C 1*s* with Gaussian fits of the wear tracks after the friction test at RT; (d) High-resolution XPS spectra of C 1*s* with Gaussian fits of the wear tracks after the friction at 400 °C; (e) High-resolution XPS spectra of O 1*s* with Gaussian fits of the wear tracks after the friction test at RT; (f) High-resolution XPS spectra of O 1*s* with Gaussian fits of the wear tracks after the friction test at 400 °C.

**Table 1**
Raman scattering results of the diamond and diamond-graphene heterostructure coatings before and after sliding.

| | Sample | D ($cm^{-1}$) | G ($cm^{-1}$) | 2D ($cm^{-1}$) | $I_D/I_G$ | $I_{2D}/I_G$ | D + D' ($cm^{-1}$) | Diamond ($cm^{-1}$) | G band ($cm^{-1}$) | $\sigma$ (*GPa*) |
|---|---|---|---|---|---|---|---|---|---|---|
| Before sliding test | Diamond | / | / | / | / | / | / | 1337 | 1563 | −2.835 |
| | Diamond-graphene | 1357 | 1589 | 2712 | 0.65 | 1.18 | 2963 | / | / | / |
| After sliding test at room temperature (center area) | Diamond | / | / | / | / | / | / | 1326 | 1523 | 3.402 |
| | Diamond-graphene | 1336 | 1574 | 2691 | 2.09 | 0.97 | 2929 | / | / | / |
| After sliding test at room temperature (edge area) | Diamond | / | / | / | / | / | / | 1327 | 1522 | 2.835 |
| | Diamond-graphene | 1334 | 1572 | 2692 | 1.91 | 0.94 | 2936 | / | / | / |
| After sliding test at 400 °C(center area) | Diamond | / | / | / | / | / | / | 1324 | 1534 | 4.536 |
| | Diamond-graphene | 1332 | 1570 | 2695 | 7.80 | 3.31 | 2937 | / | / | / |
| After sliding test at 400 °C(edge area) | Diamond | / | / | / | / | / | / | 1325 | 1526 | 3.969 |
| | Diamond-graphene | 1332 | 1571 | 2697 | 6.39 | 2.17 | 2929 | / | / | / |

from increased thermal expansion and more pronounced material deformation, which enhance stress accumulation in the coating. The diamond-graphene heterostructure coating preserves key graphene features, such as D + D′ and 2D peaks at the wear tracks, indicating the presence of graphene tribofilms that shield the friction interface from direct contact. This protective layer is absent from the pure diamond coatings. The wear tracks also show an increase in defects, as evidenced by a larger $I_D/I_G$ ratio. Structurally, the defects are more pronounced in the center than at the edges of the wear track, suggesting that graphene migrates from the center to the edges to enhance lubrication there. However, the graphene characteristics, while persisting at the edges, diminish at the center, implying that a high temperature may degrade the tribofilms in the central region through humidity-mediated oxidative processes. Despite the increased friction, the performance remains superior to that of the diamond coating.

Fig. 6c–f reveal significant changes in the C1*s* components (C–C $sp^3$, C–C $sp^2$, C–*O*–C, and C═O) and O1*s* components (C–*O*–C and C═O) at the wear tracks. After friction at RT, the $sp^2$ C–C phase is still dominant on the wear track surface of the diamond-graphene coating compared to the diamond coating (Fig. 6c–d), effectively providing lubrication phase during the sliding process. Furthermore, the higher proportion of C–*O*–C and the lower proportion of C═O oxy-functional groups in the diamond-graphene heterostructure coating suggest the formation of a stable graphene oxide lubrication layer containing epoxy groups suppressing further oxidative reactions. Conversely, the increased presence of C═O groups on the sliding interface of the diamond coating indicates a higher reactivity to facilitate the release of reactive oxygen species and promote intense oxidative reactions. Under high-temperature conditions, an increase in C═O and a decrease in C–*O*–C at the sliding interface indicate exacerbated oxidative wear compared to room temperature (Fig. 6e–f). This characteristic shift in functional groups results from humidity-dependent oxidation kinetics at elevated temperatures, promoting

C═O formation while suppressing C–*O*–C generation [79]. At high temperatures, oxygen permeates the diamond layer, significantly diminishing the $sp^3$ C–C phases and undermining the mechanical strength of the diamond coating. In contrast, the graphene layer acts as a barrier against further oxygen infiltration and helps to maintain the structural integrity and load-bearing capacity of the diamond coatings and enhance the lubricity and wear resistance. The wear mechanisms of diamond and diamond-graphene coatings at different temperatures can primarily be attributed to oxidative wear, which proceeds in two stages. Initially, the surface carbon atoms chemically adsorb oxygen from air upon heating. This is followed by the oxidation of internal carbon atoms, and it is intensified by the heat and energy generated during the friction test.

### 3.5. *Interfacial adhesion strength of diamond and diamond-graphene heterostructure coatings*

To further assess the interfacial adhesion strength and plastic deformation behavior of the diamond and diamond-graphene heterostructure coatings after subject to high temperature, the dynamical scratch tests and *in situ* optical microscope are performed, as shown in Fig. 7. Under dynamic loads from 0.3 N to 50 N, the diamond-graphene heterostructure coating exhibits robust interfacial adhesion strength compared to pure diamond coating. Specifically, the critical scratch load $L_1$ and $L_2$ of diamond coating are 3.774 N and 11.659 N, respectively, based on penetration depth (Pd) and acoustic emission (AE) signals (Fig. 7a). As shown in Fig. 7b, $L_1$ corresponds to the initiation of cracks propagation and subsequent lateral spallation. With increasing load to $L_2$, deep spallation begins, extending from the arc-shaped cracks and indicating the onset of coating failure (Fig. 7c). The diminished interfacial adhesion strength and deformation of the diamond coating can be attributed to crack propagation initiated by stress concentration at the grain boundaries, as corroborated by Raman results. At high temperatures accentuates this issue by generating thermal stress, which in turn accelerates oxidation, triggers phase transformations, and generates cyclic thermal stresses, collectively amplifying crack propagation [80]. After graphenization, the critical scratch loads $L_1$ and $L_2$ of the diamond-graphene coating are 8.166 N and 21.140 N, respectively, which is twice those of diamond coating (Fig. 7d). Obviously, the diamond-graphene coating exhibited no significant crack propagation outside the scratch and only minor cracks are observed within the scratch under the $L_1$ load (Fig. 7e). Even with the $L_2$ load, the deeper

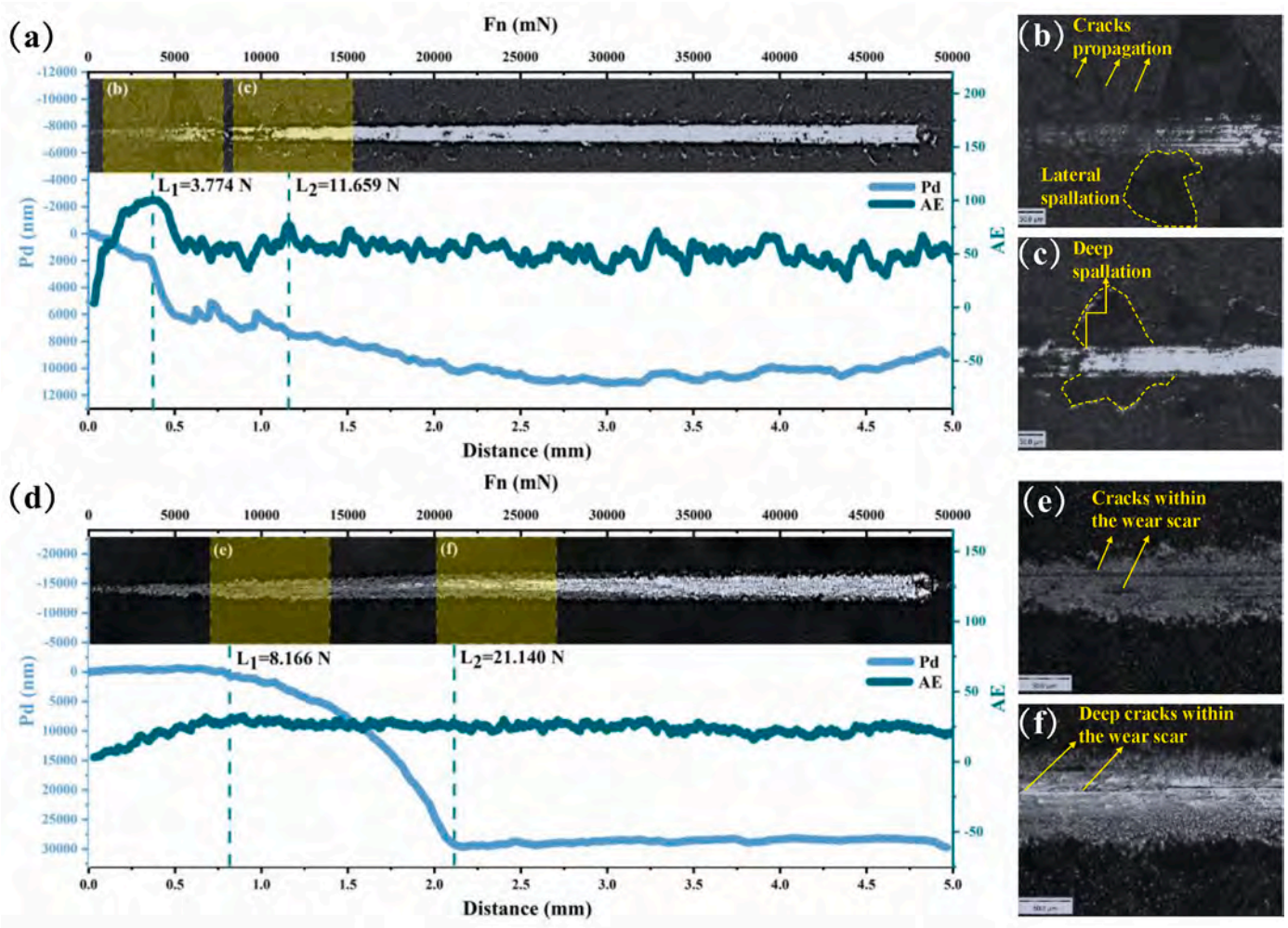


**Fig. 7.** Scratch tests of the diamond and diamond-graphene heterostructure coatings after exposure to high temperatures: (a) Curves showing changes in Pd (blue colored curve) and AE (green colored curve) against increasing normal load (Fn) and scratch distance for diamond coating (inset shows scratch grooves morphology); (b) High-magnification optical image of the diamond coating under the critical scratch load $L_1$; (c) High-magnification optical image of the diamond coating under the critical scratch load $L_2$; (d) Curves depicting variations in Pd (blue colored curve) and AE (green colored curve) against increasing Fn and scratch distance for diamond-graphene heterostructure coating (inset shows scratch grooves morphology); (e) High-magnification optical image of diamond-graphene heterostructure coating under critical scratch load $L_1$; (f) High-magnification optical image of diamond-graphene heterostructure coating under critical scratch load $L_2$. (For interpretation of the references to color in this figure legend, the reader is referred to the Web version of this article.)

scratches did not extend beyond the scratch zone, demonstrating the structural stability of the coating (Fig. 7f). Based on STEM and HR-TEM findings, the increased interfacial adhesion strength of the diamond-graphene heterostructure coating is related to the semi-coherent interface with strong covalent bonds between diamond and graphene layers. Additionally, graphene serves as a barrier to bolster the high-temperature oxidation resistance, as supported by XPS and FTIR. Consequently, the diamond-graphene coating has a more uniform stress distribution, which reduces the stress concentration points that may otherwise initiate and propagate cracks. In contrast, insufficient adhesion and oxidation resistance of the diamond coatings give rise to elastic deformation and spallation.

### 3.6. Theoretical interfacial strength and failure behaviors

To study the effects of temperature and oxidation on the mechanical properties, molecular dynamics simulations are conducted to focus on the interfacial strength and stress-strain distribution in diamond, oxidized diamond, diamond-graphene, and oxidized diamond-graphene structures at 300 K and 600 K. Fig. 8a shows the stress-strain curves of diamond and diamond-graphene structures with varying initial oxidation levels under uniaxial tension at 300 K. The abrupt stress relief in the curves represents the interfacial yield strength [81] measured at 111 GPa for diamond structure, 106 GPa for oxidized diamond structure, 128 GPa for diamond-graphene structure, and 116 GPa for oxidized diamond-graphene structure. Specifically, although diamond graphitization is generally believed to weaken the overall strength, the interfacial yield strength of the diamond-graphene structure basically matches that of pure graphene [82]. The suggests that introducing graphene layers can effectively enhance the mechanical properties of diamond due to the strong interfacial bonding between diamond and graphene. Additionally, while the interfacial yield strength of the oxidized diamond-graphene structure is lower than its non-oxidized counterpart, it remains higher than that of the diamond structure, indicating that the graphene layers enhance the diamond's mechanical properties even after oxidation. At 600 K, the interfacial yield strengths of diamond, oxidized diamond, diamond-graphene, and oxidized diamond-graphene structures decrease to 100 GPa, 103 GPa, 105 GPa,

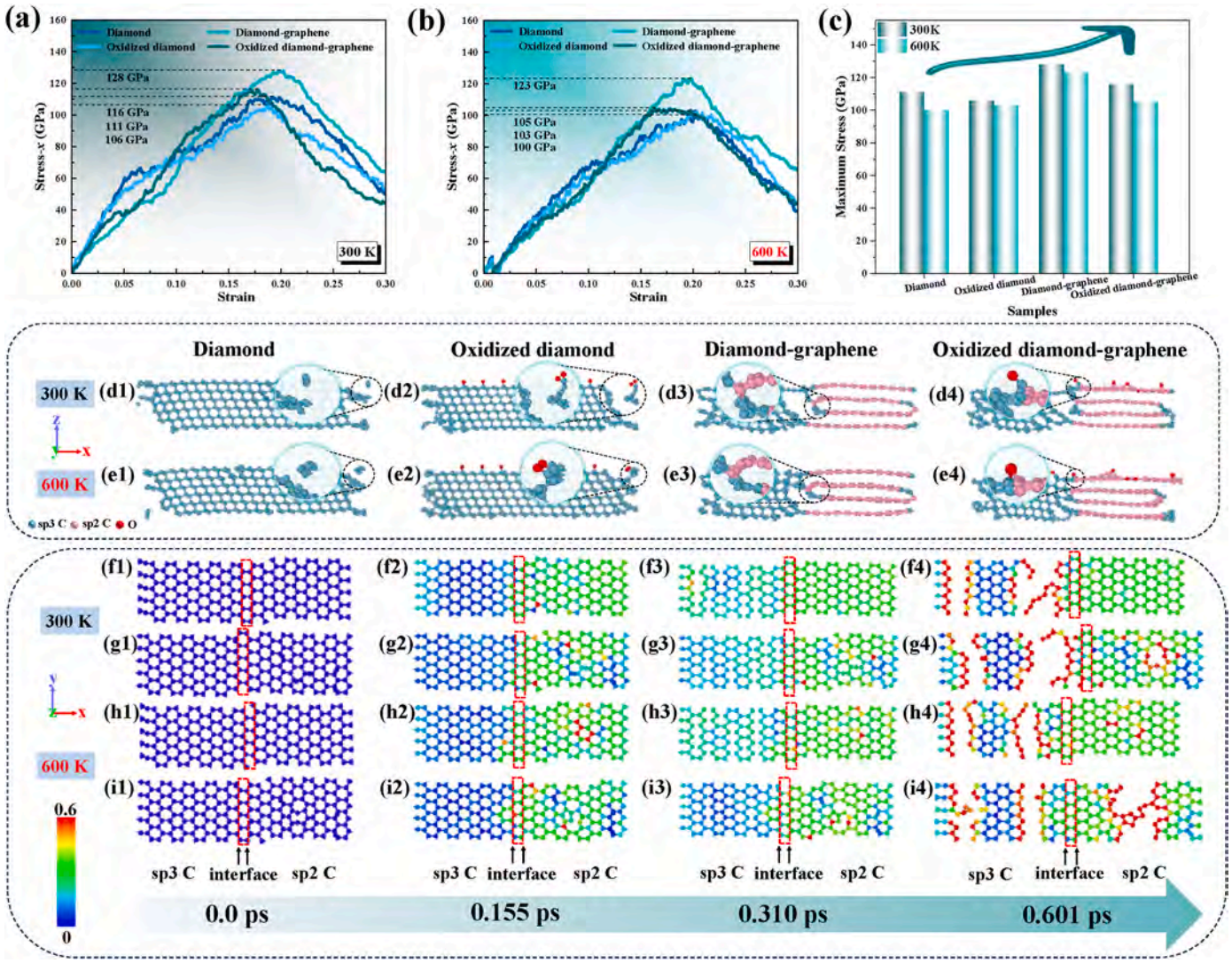


**Fig. 8.** Molecular dynamics simulation of diamond, oxidized diamond, diamond-graphene, and oxidized diamond-graphene structures: (a) Stress-strain curves during uniaxial tension process at 300 K; (b) Stress-strain curves during uniaxial tension process at 600 K; (c) Maximum stress statistics at 300 K and 600 K; (d1-d4) Atomic configurations at 0.3 strain corresponding to stress-strain curve in (a); (e1-e4) Atomic configurations at 0.3 strain corresponding to stress-strain curve in (b); Atomic strain distribution from 0 ps to 0.601 ps for (f1-f4) diamond-graphene structure at 300 K; (g1-g4) oxidized diamond-graphene structure at 300 K; (h1-h4) diamond-graphene structure at 600 K; (i1-i4) oxidized diamond-graphene structure at 600 K. A red dashed box highlights the interface region between diamond and graphene. (For interpretation of the references to color in this figure legend, the reader is referred to the Web version of this article.)

and 123 GPa, respectively (Fig. 8b). The combined effects of high temperature and oxidation slightly reduce the interfacial strength of the diamond-graphene structure, but yet it remains superior to the diamond structures (Fig. 8c), aligning with the high-temperature scratch and friction experiment results.

To further determine the failure behaviors, snapshots of the structural evolution at a strain of 0.3, corresponding to 0.601 ps, are shown in Fig. 8d1-e4. The snapshots indicate that diamond failure originates from the loss of the C atoms, which is further exacerbated under the influence of the O atoms (Fig. 8d1-d2 and Fig. 8e1-e2). The snapshots also indicate that robust bonding modulates the diamond-graphene interfacial interactions and alleviates the structural damage to carbon atoms at various temperatures (Fig. 8d3-d4 and Figs, 8e3-e4). To more clearly demonstrate the failure behaviors of the diamond-graphene structures under varying temperatures and oxidation conditions, the strain distributions at the interfaces of both diamond-graphene and oxidized diamond-graphene during the tension process are presented in Fig. 8f1-i4. As the strain increases from 0 to 0.3, corresponding to the time period from 0 ps to 0.601 ps, the structure gets slightly elongated in the interlayer region due to the breakage of C–C bonds. In the early stage of the time rising from 0 to 0.310 ps, no bond breaking is observed at the interface region, but local strain enhancement first occurs in the graphene region. At the later stage of 0.601 ps, different levels of bond breaking and crack generation indicate that the critical yield strength has been surpassed, leading to damage not confined to the interface region but also spread to the interior of the diamond and graphene lattices in the form of dislocations and tears. Notably, graphene prioritizes its own fracture internally in a self-sacrificial manner to delay the propagation of cracks within the diamond lattice. Compared to pure diamond-graphene structures (Fig. 8f1-f4 and Fig. 8h1-h4), oxygen atoms in oxidized diamond-graphene structures (Fig. 8g1-g4 and Fig. 8i1-i4) exacerbate graphene crack expansion with rising temperature, indicating high-temperature oxidation as the primary failure factor that undermines mechanical properties and thermal stability of the diamond-graphene coatings, consistent with high-temperature friction and scratch test. Specifically, the robust interface between diamond and graphene facilitates energy and stress transfer, enabling the flexible graphene to adjust elastically and dissipate stress before the brittle diamond succumbs to catastrophic failure. This enhances the overall resistance of the diamond-graphene structure to high-temperature oxidation and friction.

### 3.7. Theoretical surface oxidation resistance properties and mechanisms

To elucidate the critical mechanisms by which graphene affects the antioxidative properties of diamond surfaces, the interactions between carbon and oxygen atoms on defective diamond and diamond-graphene surfaces are investigated by DFT calculations (Fig. 9). To investigate the bonding stability of O atom adsorbing on the surface of defective diamond and diamond-graphene structures both with specific C atomic vacancy, the $E_{ads}$ values are calculated and the adsorption structures shown in Fig. 9a. Single O atom preferentially adsorbs on the C atom in defective diamond structure, whereas in defective diamond-graphene structure, O atom tends to adsorb at central vacancy sites surrounded by three C atoms, indicating the formation of stable epoxy groups. A larger absolute $E_{ads}$ means stronger oxidative bonding stability [83]. The defective diamond and diamond-graphene structures exhibit absolute $E_{ads}$ values of 0.1211 eV and 0.2702 eV, respectively, indicating enhanced surface carbon-oxygen bonding interaction in the defective diamond-graphene structure. Graphene defects act as preferential sacrifice sites for capturing and adsorbing oxygen atoms and form stable carbon-oxygen bonds, thereby preventing additional oxygen diffusion into the interior. In line with the XPS results, this interaction forms a stable graphene oxide layer with epoxy groups on the surface, which

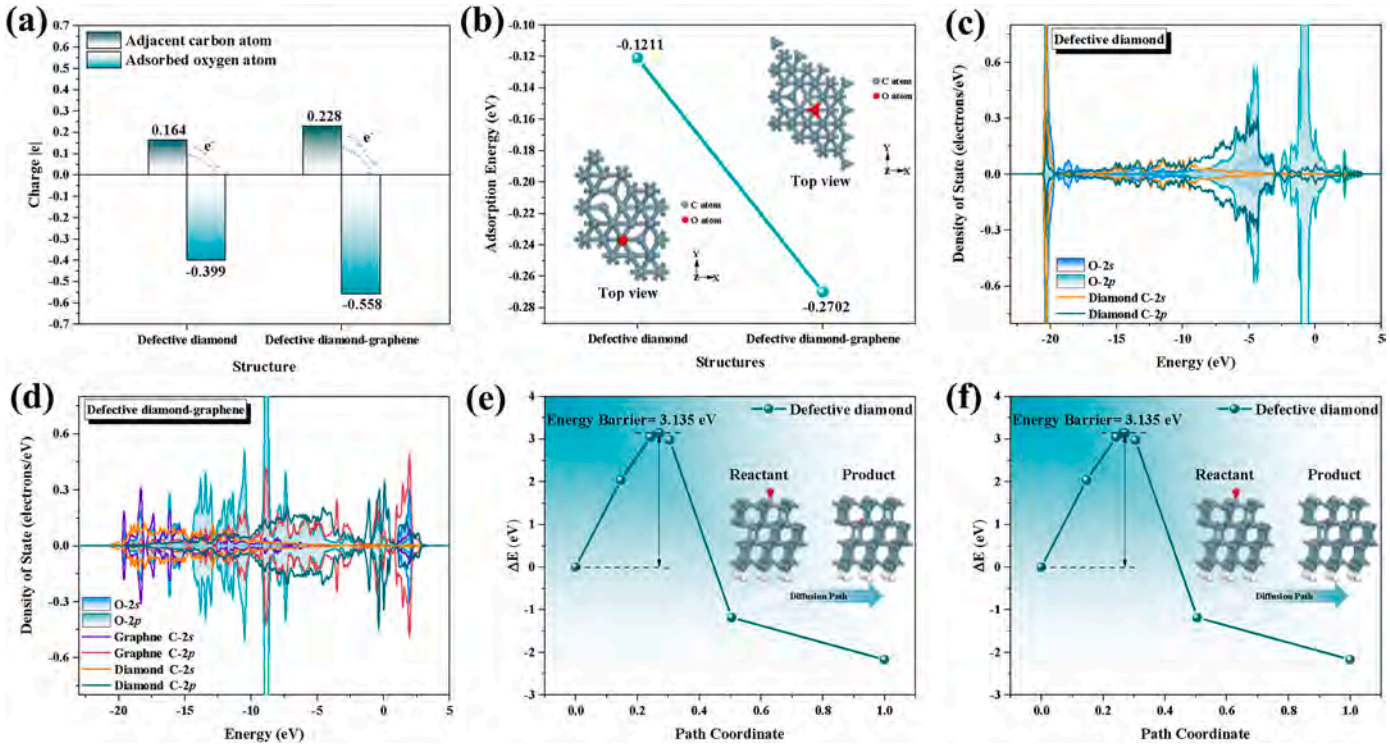


**Fig. 9.** DFT calculations for defective diamond and diamond-graphene structures: (a) Adsorption energy (top views of the structures are depicted in the insert); (b) Charge distribution of the adsorbed oxygen atom and adjacent carbon atom; (c) PDOS characterization of the C-2*s*, C-2*p*, O-2*s*, and O-2*p* orbitals for C and O atoms in the defective diamond structure; (d) PDOS characterization of the C-2*s*, C-2*p*, O-2*s*, and O-2*p* orbitals for C and O atoms in the defective diamond-graphene structure; Calculated diffusion energy barriers for one O atom diffusing from reactant to product states in (e) the defective diamond structure and (f) the defective diamond-graphene structure (side views of the reactant and product are shown in the insets). (A colour version of this figure can be viewed online.)

only undergoes further chemical reactions under specific conditions. To understand the surface adsorption enhancement, the electronic structure perspective is shown in Fig. 9b. A higher Mulliken population signifies stronger polar bonds [84]. The charges of the adsorbed oxygen atom are 0.164|e| in the defective diamond structure and 0.228|e| in the defective diamond-graphene structure, while for the adjacent carbon atom, they are 0.399|e| and 0.558|e|, respectively. The greater charge accumulation on the oxygen atom in the defective diamond-graphene structure is key evidence of strengthened carbon-oxygen bonding resulting from increased electron cloud overlap.

The density of states (DOS) is calculated to further assess the interaction between O atoms and C atoms, as shown in Fig. 9c–d. The overlapping of multiple orbitals signifies covalent bond formation, while the energy fluctuations represent substantial hybridization among these orbitals [85]. In the defective diamond structure, overlapping regions occur between the C-2*s*, C-2*p*, O-2*s* and O-2*p* orbitals, indicating interaction within the carbon-oxygen bonds (Fig. 9c). There is more extensive overlapping between the O-2*s* and O-2*p* orbitals and the C-2*s* and C-2*p* orbitals from graphene compared to those from diamond, suggesting stronger carbon-oxygen bond interactions in defective graphene layer but weaker interactions in defective diamond (Fig. 9d). This phenomenon arises due to the highly electronegative O atoms readily form strong bonds with the unpaired electrons and high electron density areas at graphene defect sites before bonding with C atoms in defective diamond. Further calculations on the oxygen diffusion energy barrier in the defective diamond structure with and without defective graphene layer are performed to evaluate the effects of defective graphene on the oxidation resistance of defective diamond during the later stage of oxidation. As shown in Fig. 9e–f, the arrows in the inset depict the diffusion path of the O atom from stable reactant to product. In the case of the defective diamond, the energy barrier for the O atom permeation into the diamond interior is 3.135 eV (Fig. 9e), whereas it increases to 13.029 eV when a defective graphene layer is covered (Fig. 9f). The elevated diffusion energy barrier suggests that O atom diffusion in the defective diamond-graphene structure is significantly more difficult than in the defective diamond structure. The graphene surface, characterized by its active defect sites and lower surface energy, effectively captures O atoms and forms strong carbon-oxygen bonds. Disrupting these bonds requires substantial energy, highlighting the stability of the bonding. Consequently, oxygen diffusion on the graphene-covered diamond surface encounters a significantly higher energy barrier compared to the defective diamond structure. According to the calculation results, the significantly improved oxidation resistance of the diamond-graphene structure can be attributed to the restricted diffusion of O atoms on the graphene-covered surface.

The schematic diagram in Fig. 10 illustrates the inherent relationships between the diamond-graphene heterostructure coatings and their friction and oxidation resistance properties. Graphene forms a robust interface with the underlying diamond, enabling the flexible graphene layer in a self-sacrificial manner to transfer and dissipate energy before the brittle diamond experiences crack propagation and catastrophic failure. This maintains the high load-bearing capacity and excellent mechanical properties of diamond to enhance the wear resistance. Defective graphene serves as sacrificial sites that preferentially capture and facilitate the adsorption of oxygen atoms from frictional heating and the ambient environment. This results in the formation of a lubricative graphene oxide layer with stable carbon-oxygen bonds on the surface, which effectively prevents direct contact at the friction interface and enhances lubrication [86]. Specifically, strong carbon-oxygen bonds create diffusion barriers to inhibit oxygen atoms from bonding with internal diamond carbon atoms and prevent oxygen penetration into the bulk of the diamond. This contributes significantly to the outstanding oxidation resistance of the diamond-graphene heterostructure coatings. Therefore, the diamond-graphene heterostructure coatings demonstrate superior friction and oxidation resistance at elevated temperatures, attributed to the synergistic enhancement of interfacial strength and oxygen diffusion energy barrier.

## 4. Conclusions

Friction and oxidation resistance are demonstrated for the diamond-graphene heterostructure coatings with semi-coherent interface. Experimental and theoretical calculations results reveal the interfacial interaction between diamond and graphene and their friction and oxidation behavior. The semi-coherent interfaces marked by regions of robust bonding interspersed with dislocation defects are *in situ* fabricated in diamond-graphene heterostructure coatings. The robust bonding interfaces facilitate effective energy and stress transfer, thereby allowing the flexible graphene in a self-sacrificial manner to adjust elastically and stress dissipation before the brittle diamond undergoes crack propagation and catastrophic failure. In addition, the engineered defects within graphene layers serve as active sites for oxygen adsorption, resulting in a high-energy barrier against oxygen diffusion into the deeper diamond matrix. Furthermore, the graphene oxide layer with stable C–O bonds prevents direct contact and enable interlayer shear sliding at the friction interface. Benefiting from the enhanced adhesion

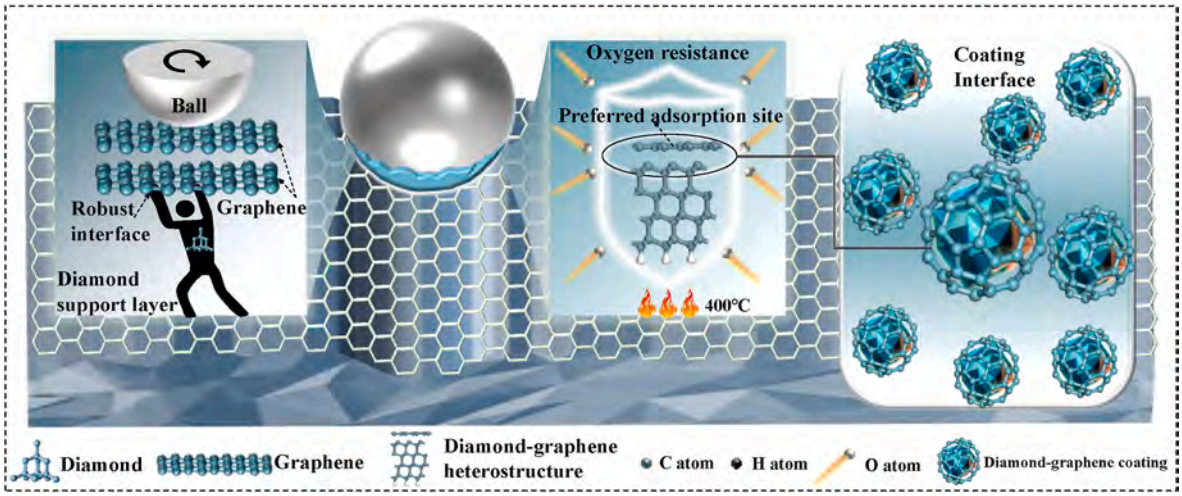


**Fig. 10.** Schematic illustration of the diamond-graphene heterostructure coating mechanisms showing the robust interface formation between diamond and graphene layer for improved friction resistance, and the preferential oxygen adsorption on graphene surface sites for enhanced oxidation resistance. (A colour version of this figure can be viewed online.)

strength and oxygen resistance, diamond-graphene heterostructure coatings demonstrate over 35 % improvement in the friction properties at various temperatures compared to diamond coatings. This study elucidates the mechanisms for the enhanced friction and oxidation resistance in diamond-graphene heterostructure coatings and reveal a promising strategy for high-temperature friction applications.

## CRediT authorship contribution statement

**Shuyu Fan:** Writing – review & editing, Writing – original draft, Visualization, Validation, Methodology, Investigation, Formal analysis, Data curation, Conceptualization. **Shu Xiao:** Writing – review & editing, Writing – original draft, Supervision, Resources, Project administration, Funding acquisition, Conceptualization. **Hu Zhang:** Visualization, Validation, Methodology, Investigation, Formal analysis, Data curation. **Songsheng Lin:** Writing – review & editing, Supervision, Resources, Project administration, Funding acquisition, Conceptualization. **Jing Wu:** Validation, Methodology, Investigation, Data curation. **Fenghua Su:** Supervision, Resources, Project administration. **Paul K. Chu:** Supervision, Resources, Project administration, Funding acquisition.

## Declaration of competing interest

The authors declare that they have no known competing financial interests or personal relationships that could have appeared to influence the work reported in this paper.

## Acknowledgments

This work is supported by the National Natural Science Foundation of China (No. 52375182 and No. 52005187), Natural Science Foundation of Guangdong Province (No. 2023A1515012308), Guangdong Province Science and Technology Plan Projects (No. 2023B1212060045 and No. 2023B1212120008), Basic and Applied Basic Research Fund of Guangdong Province (No. 2024A1515010452), as well as City University of Hong Kong Donation Research Grants (No. DON-RMG 9229021 and No. 9229021).

## Appendix A. Supplementary data

Supplementary data to this article can be found online at https://doi.org/10.1016/j.carbon.2025.120072.

## References

[1] J.B. Lou, M. Liu, L.R. Ma, Origin of friction and the new frictionless technology-Superlubricity: advancements and future outlook, Nano Energy 86 (2021) 106092.
[2] K. Holmberg, A. Erdemir, Influence of tribology on global energy consumption, costs and emissions, Friction 5 (3) (2017) 263–284.
[3] R. Rejith, D. Kesavan, P. Chakravarthy, S.V.S.N. Murty, Bearings for aerospace applications, Tribol. Int. 181 (2023) 108312.
[4] H. Peng, H. Zhang, L. Shangguan, Y. Fan, Review of tribological failure analysis and lubrication technology research of wind power bearings, Polymers 14 (15) (2022) 3041.
[5] M. John, P.L. Menezes, Self-lubricating materials for extreme condition applications, Materials 14 (19) (2021) 5588.
[6] S.Y. Fan, Y.N. Chen, S. Xiao, K.J. Shi, X.Y. Meng, S.S. Lin, F.H. Su, Y.F. Su, P.K. Chu, In situ self-adaptive growth of graphene coatings on hard substrates via competitive NiCo catalysis reaction, Carbon 216 (2024) 118561.
[7] S.Y. Fan, Y.N. Chen, J. Wu, S. Xiao, G.H. Chen, P.K. Chu, Structure, superlubricity, and applications of graphene solid lubricants prepared by chemical vapor deposition, Tribol. Int. 198 (2024) 109896.
[8] H. Zhang, H. Song, M. Pang, G.Y. Yang, F.Q. Ji, N. Jiang, K. Nishimura, Tribological performance of microcrystalline diamond (MCD) and nanocrystalline diamond (NCD) coating in dry and seawater environment, Crystals 12 (10) (2022) 1345.
[9] D. Berman, A. Erdemir, A.V. Sumant, Graphene: a new emerging lubricant, Mater. Today 17 (1) (2013) 31–42.
[10] S.Y. Fan, S. Xiao, S.S. Lin, F.H. Su, Y.F. Su, P.K. Chu, Macroscale superlubricity and durability of in situ grown hydrogenated graphene coatings, Chem. Eng. J. 459 (2023) 141521.
[11] C. Kumara, M.J. Lance, J. Qu, Macroscale superlubricity by a sacrificial carbon nanotube coating, Mater. Today Nano 21 (2023) 100297.
[12] L.Q. Peng, H.T. Yu, C. Chen, Q.X. He, H. Zhang, F.L. Zhao, M.M. Qin, Y.Y. Feng, W. Feng, Tailoring dense, orientation-tunable, and interleavedly structured carbon-based heat dissipation plates, Adv. Sci. 10 (7) (2023) 2205962.
[13] Z. Li, Y. Wang, M. Ma, H.C. Ma, W.T. Hu, X. Zhang, Z.W. Zhuge, S.S. Zhang, K. Luo, Y.F. Gao, L. Sun, A.V. Soldatov, Y.J. Wu, B. Liu, B.Z. Li, P. Ying, Y. Zhang, B. Xu, J. He, D.L. Yu, Z.Y. Liu, Z.S. Zhao, Y.Z. Yue, Y.J. Tian, X.Y. Li, Ultrastrong conductive in situ composite composed of nanodiamond incoherently embedded in disordered multilayer graphene, Nat. Mater. 22 (1) (2023) 42–49.
[14] J.F. Archard, Contact and rubbing of flat surfaces, J. Appl. Phys. 24 (1953) 981–988.
[15] A. Shekhawat, R.O. Ritchie, Toughness and strength of nanocrystalline graphene, Nat. Commun. 7 (1) (2016) 10546.
[16] S. Zhao, K. Larsson, First principle study of the attachment of graphene onto non-doped and doped diamond (111), Diam. Relat. Mater. 66 (2016) 52–60.
[17] D. Berman, S.A. Deshmukh, B. Narayanan, S.K.R.S. Sankaranarayanan, Z. Yan, A. A. Balandin, A. Zinovev, D. Rosenmann, A.V. Sumant, Metal-induced rapid transformation of diamond into single and multilayer graphene on wafer scale, Nat. Commun. 7 (1) (2016) 1–8.
[18] B. Shen, Z. Ji, Q. Lin, P. Gong, N.N. Xuan, S.L. Chen, H.Q. Liu, Z.W. Huang, T. X. Xiao, Z.Z. Sun, Graphenization of diamond, Chem. Mater. 34 (9) (2022) 3941–3947.
[19] C. Zhang, R.D. Vispute, K. Fu, C.Y. Ni, A review of thermal properties of CVD diamond films, J. Mater. Sci. 58 (8) (2023) 3485–3507.
[20] Y.F. Fu, J. Hansson, Y. Liu, S.J. Chen, A. Zehri, M.K. Samani, N. Wang, Y.X. Ni, Graphene related materials for thermal management, 2D Mater. 7 (2019) 012001.
[21] C. Lu, Z. Li, S. Li, Z. Li, Y.Y. Zhang, J.H. Zhao, Molecular dynamics study of thermal transport properties across covalently bonded graphite-nanodiamond interfaces, Carbon 213 (2023) 118250.
[22] J. Vejpravová, Mixed sp2–sp3 nanocarbon materials: a status quo review, Nanomaterials 11 (10) (2021) 2469.
[23] Q. Lin, S.L. Chen, Z. Ji, B. Shen, Covalent graphene-diamond heterostructure coating on tool surface with enhanced lubricity and anti-wear performance, Carbon 217 (2024) 118648.
[24] Y.T. Zhu, K. Ameyama, P.M. Anderson, I.J. Beyerlein, H.J. Gao, H.S. Kim, E. Lavernia, S. Mathaudhu, H. Mughrabi, R.O. Ritchie, N. Tsuji, X.Y. Zhang, X. L. Wu, Heterostructured materials: superior properties from hetero-zone interaction, Mater. Res. Lett 9 (1) (2021) 1–31.
[25] S. Zhu, X. Yan, J. Liu, et al., A revisited mechanism of the graphite-to-diamond transition at high temperature, Matter 3 (3) (2020) 864–878.
[26] Y.P. Xie, X.J. Zhang, Z.P. Liu, Graphite to diamond: origin for kinetics selectivity, J. Am. Chem. Soc. 139 (7) (2017) 2545–2548.
[27] L. Fan, J. Xu, Y.H. Hong, Defects in graphene-based heterostructures: topological and geometrical effects, RSC Adv. 12 (11) (2022) 6772–6782.
[28] S. Chen, Q. Lin, Z. Ji, Z.Z. Sun, B. Shen, Ultrahigh mechanical robustness of vertical graphene sheets covalently bonded to diamond, Carbon 201 (2023) 390–398.
[29] D. Berman, S.A. Deshmukh, S.K.R.S. Sankaranarayanan, A. Erdemir, A.V. Sumant, Macroscale superlubricity enabled by graphene nanoscroll formation, Science 348 (6239) (2015) 1118–1122.
[30] Z. Ji, Q. Lin, Z.W. Huang, S.L. Chen, P. Gong, Z.Z. Sun, Enhanced lubricity of CVD diamond films by in-situ synthetization of top-layered graphene sheets, Carbon 184 (2021) 680–688.
[31] S. Fan, T.C. Kuang, W. Xu, Y.M. Zhang, Y.F. Su, S.S. Lin, D. Wang, H.Z. Yang, K. S. Zhou, M.J. Dai, L. Wang, Effect of pretreatment strategy on the microstructure, mechanical properties and cutting performance of diamond coated hardmetal tools using HFCVD method, Int. J. Refract. Met. Hard Mater. 101 (2021) 105687.
[32] J.M. Garcia, R. He, M.P. Jiang, P. Kim, L.N. Pfeiffer, A. Pinczuk, Multilayer graphene grown by precipitation upon cooling of nickel on diamond, Carbon 49 (2011) 1006–1012.
[33] Z. Ji, Q. Lin, Z.W. Huang, S.L. Chen, P. Gong, Z.Z. Sun, T.B. Li, J.A., Enhanced lubricity of CVD diamond films by in-situ synthetization of top-layered graphene sheets, Carbon 184 (2021) 680–688.
[34] B. Shen, S.L. Chen, Y. Chen, F.H. Sun, Enhancement on the tribological performance of diamond films by utilizing graphene coating as a solid lubricant, Surf. Coat. Technol. 311 (2017) 35–45.
[35] Z.Y. Shi, Z.J. Jin, X.G. Gua, X.L. Shi, J. Guo, Interfacial friction properties in diamond polishing process and its molecular dynamic analysis, Diam. Relat. Mater. 100 (2019) 107546.
[36] X.Z. Zeng, Y.T. Peng, L. Liu, H.J. Lang, X. Cao, Dependence of the friction strengthening of graphene on velocity, Nanoscale 10 (2018) 1855.
[37] S. Plimpton, Fast parallel algorithms for short-range molecular dynamics, J. Comput. Phys. 117 (1) (1995) 1–19.
[38] M. Kowalik, C. Ashraf, B. Damirchi, D. Akbarian, S. Rajabpour, A.C.T.V. Duin, Atomistic scale analysis of the carbonization process for C/H/O/N-based polymers with the ReaxFF reactive force field, J. Phys. Chem. B 123 (2019) 5357–5367.
[39] B. Delley, An all-electron numerical method for solving the local density functional for polyatomic molecules, J. Chem. Phys. 92 (1) (1990) 508–517.
[40] J.P. Perdew, K. Burke, M. Ernzerhof, Generalized gradient approximation made simple, Phys. Rev. Lett. 78 (7) (1997) 1396, 1396.
[41] J.P. Perdew, J.A. Chevary, S.H. Vosko, K.A. Jackon, M.R. Pederson, D.J. Singh, C. Fiolhais, Atoms, molecules, solids, and surfaces: applications of the generalized gradient approximation for exchange and correlation, Phys. Rev. B 46 (11) (1992) 6671–6687.
[42] S. Grimme, Semiempirical GGA-type density functional constructed with a long-range dispersion correction, J. Comput. Chem. 27 (15) (2006) 1787–1799.

[43] T.A. Halgren, W.N. Lipscomb, The synchronous-transit method for determining reaction pathways and locating molecular transition states, Chem. Phys. Lett. 49 (1977) 225–232.
[44] C.Y. Cheng, H.J. Li, Q.G. Fu, L. Li, L.P. Guo, Influence of $Al_2O_3$ on the oxidation resistance of SiC ceramic: first-principle study and experiment, Corros. Sci. 134 (2018) 57–63.
[45] D. Sanchez-Portal, E. Artacho, J.M. Soler, Projection of plane-wave calculations into atomic orbitals, Solid State Commun 95 (1995) 685–689.
[46] R.S. Mulliken, Electronic population analysis on LCAO-MO molecular wave functions I, J. Chem. Phys. 23 (1995) 1833.
[47] P. Dai, Z. Wei, L. Chen, Y. Liu, Adsorption of butyl xanthate on arsenopyrite (001) and Cu2+-activated arsenopyrite (001) surfaces: a DFT study, Chem. Phys. 562 (2022) 111668.
[48] C.L. Wang, M.F. Li, C.G. Zhou, Insight into the effect of Ge modification on the oxidation of $NbSi_2$ from first-principles calculations, Prog. Nat. Sci. 31 (2021) 618–623.
[49] F. Lavini, M. Rejhon, E. Riedo, Two-dimensional diamonds from sp2-to-sp3 phase transitions, Nat. Rev. Mater. 7 (2022) 814–832.
[50] R. Arenal, P. Bruno, D.J. Miller, M. Bleuel, J. Lal, D.M. Gruen, Diamond nanowires and the insulator-metal transition in ultrananocrystalline diamond films, Phys. Rev. B 75 (2007) 195431.
[51] J.F. Morar, F.J. Himpsel, G. Hollinger, G. Hughes, J.L. Jordan, Observation of a C-1s core exciton in diamond, Phys. Rev. Lett. 54 (1985) 1960–1963.
[52] B. Yan, N. Chen, Y. Zhu, Y.F. Yang, G.L. Zhao, W. Zhao, X.Q. Hao, L. Li, L. Wang, E. Abele, N. He, Instantaneous formation of covalently bonded diamond–graphite–graphene with synergistic properties, Int. J. Mach. Tools Manuf. 193 (2023) 104087.
[53] G. Pilania, P.P. Dholabhai, B.P. Uberuaga, Role of Symmetry, geometry, and termination chemistry on misfit dislocation patterns at semicoherent heterointerfaces, Matter 2 (5) (2020) 1324–1337.
[54] S.C. Li, H.Y. Liang, C. Li, Y.C. Liu, Lattice mismatch in $Ni_3Al$-based alloy for efficient oxygen evolution, J. Mater. Sci. Technol. 106 (2022) 19–27.
[55] T.B. Li, J.A. Yarmoff, Defect-induced oxygen adsorption on graphene films, Surf. Sci. 675 (2018) 70–77.
[56] M.D. Bhatt, H. Kim, G. Kim, Various defects in graphene: a review, RSC Adv 12 (2022) 21520.
[57] P. Németh, K. McColl, R.L. Smith, M. Murri, L.A.J. Garvie, M. Alvaro, B. Pécz, A. P. Jones, F. Corà, C.G. Salzmann, P.F. McMillan, Diamond-graphene composite nanostructures, Nano Lett. 20 (5) (2020) 3611–3619.
[58] J.W. Xiao, H.Z. Yang, X.Z. Wu, F. Younus, P. Li, B. Wen, X.Y. Zhang, Y.B. Wang, Y. J. Tian, Dislocation behaviors in nanotwinned diamond, Sci. Adv. 4 (9) (2018) eaat8195.
[59] F.H. Su, K. Yao, Facile fabrication of superhydrophobic surface with excellent mechanical abrasion and corrosion resistance on copper substrate by a novel method, ACS Appl. Mater. Interfaces 6 (11) (2014) 8762–8770.
[60] S. Bhowmick, A. Banerji, A.T. Alpas, Role of humidity in reducing sliding friction of multilayered graphene, Carbon 87 (2015) 374–384.
[61] S.P. Cooil, J.W. Wells, D. Hu, Y.R. Niu, A.A. Zakharov, M. Bianchi, D.A. Evans, Controlling the growth of epitaxial graphene on metalized diamond (111) surface, Appl. Phys. Lett. 107 (18) (2015) 181603.
[62] L. Bergman, R.J. Nemanich, Raman and photoluminescence analysis of stress state and impurity distribution in diamond thin films, J. Appl. Phys. 78 (1995) 6709–6719.
[63] J.B. Wu, M.L. Lin, X. Cong, H.N. Liu, P.H. Tan, Raman spectroscopy of graphene-based materials and its applications in related devices, Chem. Soc. Rev. 47 (5) (2018) 1822–1873.
[64] M.R. Anisur, P.C. Banerjee, C.D. Easton, R.K.S. Raman, Controlling hydrogen environment and cooling during CVD graphene growth on nickel for improved corrosion resistance, Carbon 127 (2017) 131–140.
[65] V. Tucureanu, A. Matei, A.M. Avram, FTIR spectroscopy for carbon family study, Crit. Rev. Anal. Chem. 46 (6) (2016) 502–520.
[66] M.S. Bhutta, X.B. Tang, S. Akram, Y.D. Chen, X.C. Ren, M. Fasehullah, G. Rasool, T. Nazir, Development of novel hybrid 2D-3D graphene oxide diamond micro composite polyimide films to ameliorate electrical & thermal conduction, J. Ind. Eng. Chem. 114 (2022) 108–114.
[67] A.B. Puthirath, E.F. Oliveira, G.H. Gao, N. Chakingal, H. Kannan, C.X. Li, X. Zhang, A. Biswas, M.R. Neupane, B.B. Pate, D.A. Ruzmetoz, A.G. Birdwell, T.G. Ivanov, D. S. Galvao, R. Vajtai, P.M. Ajayan, Oxygenation of diamond surfaces via hummer's method, Chem. Mater. 33 (13) (2021) 4977–4987.
[68] N.F. Chiu, C.D. Yang, Real-time and stepwise deoxidization processes to tune the photoluminescence properties of graphene oxide using EC-SPR spectroscopy, RSC Adv 8 (21) (2018) 11557–11565.
[69] J. Hintikka, A. Mäntylä, J. Vaara, T. Vaara, J. Juoksukangas, A. Lehtovaara, Running-in in fretting, transition from near-stable friction regime to gross sliding, Tribol. Int. 143 (2020) 106073.
[70] S.Y. Zhu, J. Cheng, Z.H. Qiao, J. Yang, High temperature solid-lubricating materials: a review, Tribol. Int. 133 (2019) 206–223.
[71] J. Wei, P. Guo, H. Li, P.L. Ke, A.Y. Wang, Insights on high temperature friction mechanism of multilayer ta-C films, J. Mater. Sci. Technol. 97 (2022) 29–37.
[72] Y.S. Geng, J. Cheng, H. Tan, Q.C. Sun, J.J. Chen, S.Y. Zhu, A.K. Tieu, J. Yang, W. M. Liu, A $(CrFeNi)_{83}(AlTi)_{17}$ high-entropy alloy matrix solid-lubricating composite with exceptional tribological properties over a wide temperature range, J. Mater. Sci. Technol. 153 (2023) 75–91.
[73] O. Jantschner, S.K. Field, D. Holec, A. Fian, D. Music, J.M. Schneider, K. Zorn, C. Mitterer, Origin of temperature-induced low friction of sputtered Si-containing amorphous carbon coatings, Acta Mater 82 (2015) 437–446.
[74] J.H. Ouyang, Y.F. Li, Y.Z. Zhang, Y.M. Wang, Y.J. Wang, High-temperature solid lubricants and self-lubricating composites: a critical review, Lubricants 10 (8) (2022) 177.
[75] R. Kumar, I. Hussainova, R. Rahmani, M. Antonov, Solid lubrication at high-temperatures—a review, Materials 5 (15) (2022) 1695.
[76] M.H. Rahman, H. Warneke, H. Webbert, J. Rodriguez, E. Austin, K. Tokunaga, D. K. Rajak, P.L. Menezes, Water-based lubricants: development, properties, and performances, Lubricants 9 (8) (2021) 73.
[77] A. Hai, S.S. Li, J.Q. He, S.F. He, H.Y. Dai, X.B. Liu, J.L. Sun, Z.C. Dong, L. Jiang, High-temperature wettable water-based lubricants toward hot rolling lubrication, Adv. Funct. Mater. 34 (2024) 2316793.
[78] P. Kumar, V.K. Srivastava, A review on wear and friction performance of carbon–carbon composites at high temperature, Int. J. Appl. Ceram. Technol. 13 (4) (2016) 702–710.
[79] B. Liu, H.J. Sun, T.J. Peng, J.Z. Yang, Y.Z. Ren, J. Ma, G.P. Tang, L.L. Wang, S. K. Huang, High selectivity humidity sensors of functionalized graphite oxide with more epoxy groups, Appl. Surf. Sci. 503 (15) (2020) 144312.
[80] A. Bird, L. Yang, G. Wu, B.J. Inkson, Failure mechanisms of diamond like carbon coatings characterized by in situ SEM scratch testing, Wear 530 (2023) 205034.
[81] L.F. Tomilin, S.V. Erohin, N.A. Nebogatikova, I.V. Antonova, A.K. Gutakovskii, V. A. Volodin, E.A. Korneeva, P.B. Sorokin, 2D diamond structures in multilayer graphene: simulation and experimental observation, Carbon 220 (2024) 118832.
[82] C.G. Lee, X.D. Wei, J.W. Kysar, J. Hone, Measurement of the elastic properties and intrinsic strength of monolayer graphene, Science. 321 (5887) (2008) 385–388.
[83] X. Chen, L. Xu, L.L. Liu, L.S. Zhao, C.P. Chen, Y. Zhang, X.C. Wang, Adsorption of formaldehyde molecule on the pristine and transition metal doped graphene: first-principles study, Appl. Surf. Sci. 396 (2017) 1020–1025.
[84] L.L. Zhao, S.D. Pan, G. Frenking, The nature of the polar covalent bond, J. Chem. Phys. 157 (3) (2022) 034105.
[85] R. Nelson, C. Ertural, J. George, V.L. Deringer, G. Hautier, R. Dronskowski, LOBSTER: local orbital projections, atomic charges, and chemical-bonding analysis from projector-augmented-wave-based density-functional theory, J. Comput. Chem. 41 (21) (2020) 1931–1940.
[86] S.Z. Li, Q.Y. Li, R.W. Carpick, P. Gumbsch, X.Z. Liu, X.D. Ding, J. Sun, J. Li, The evolving quality of frictional contact with graphene, Nature 539 (2016) 541–545.

Carbon 237 (2025) 120129

Contents lists available at ScienceDirect

Carbon

journal homepage: www.elsevier.com/locate/carbon

Corrigendum

# Corrigendum to "High-temperature friction and oxidation resistance of self-sacrificial diamond-graphene heterostructures coatings" [Carbon 235 (2025) 120072]

Shuyu Fan [a,b], Shu Xiao [a,*], Hu Zhang [a], Songsheng Lin [b,**], Jing Wu [a], Fenghua Su [a], Paul K. Chu [c]

[a] School of Mechanical & Automotive Engineering, South China University of Technology, Guangzhou, 510641, China
[b] Guangdong-Hong Kong Joint Laboratory of Modern Surface Engineering Technology, Guangdong Provincial Key Laboratory of Modern Surface Engineering Technology, Institute of New Materials, Guangdong Academy of Sciences, Guangzhou, 510651, China
[c] Department of Physics, Department of Materials Science and Engineering, and Department of Biomedical Engineering, City University of Hong Kong, Tat Chee Avenue, Kowloon, Hong Kong, China

The authors regret the error < We recently identified image errors in our paper, published online on February 5th, 2025. During the revision process, two formatting issues occurred due to figure reformatting: (1) an image was inadvertently duplicated in Fig. 9f–and (2) Fig. 9a and b were accidently transposed, though their captions and text content remain correct. These errors are purely formatting-related and occurred during the preparation of the revised manuscript. To address these issues, we propose replacing Fig. 9f with the correct image from our original submission and restoring the proper order of Fig. 9a and b to align with their captions and text content. These corrections do not affect any results or conclusions presented in the manuscript>. The corrected image part is provided below:

The corrected image in manuscript Fig. 9f is shown below:

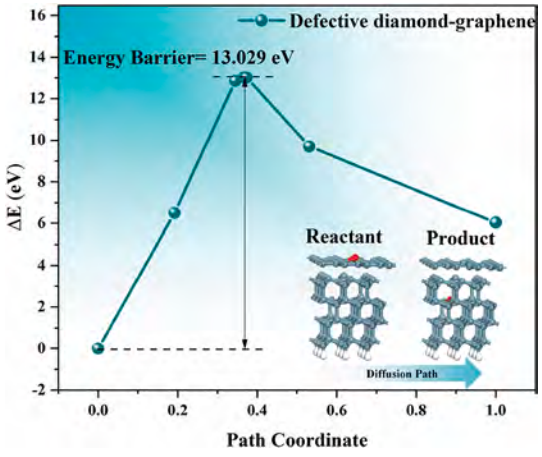


The corrected version in manuscript Fig. 9 is shown below:

DOI of original article: https://doi.org/10.1016/j.carbon.2025.120072.
* Corresponding author.
** Corresponding author.
*E-mail address:* xiaos@scut.edu.cn (S. Xiao).

https://doi.org/10.1016/j.carbon.2025.120129

Available online 22 February 2025

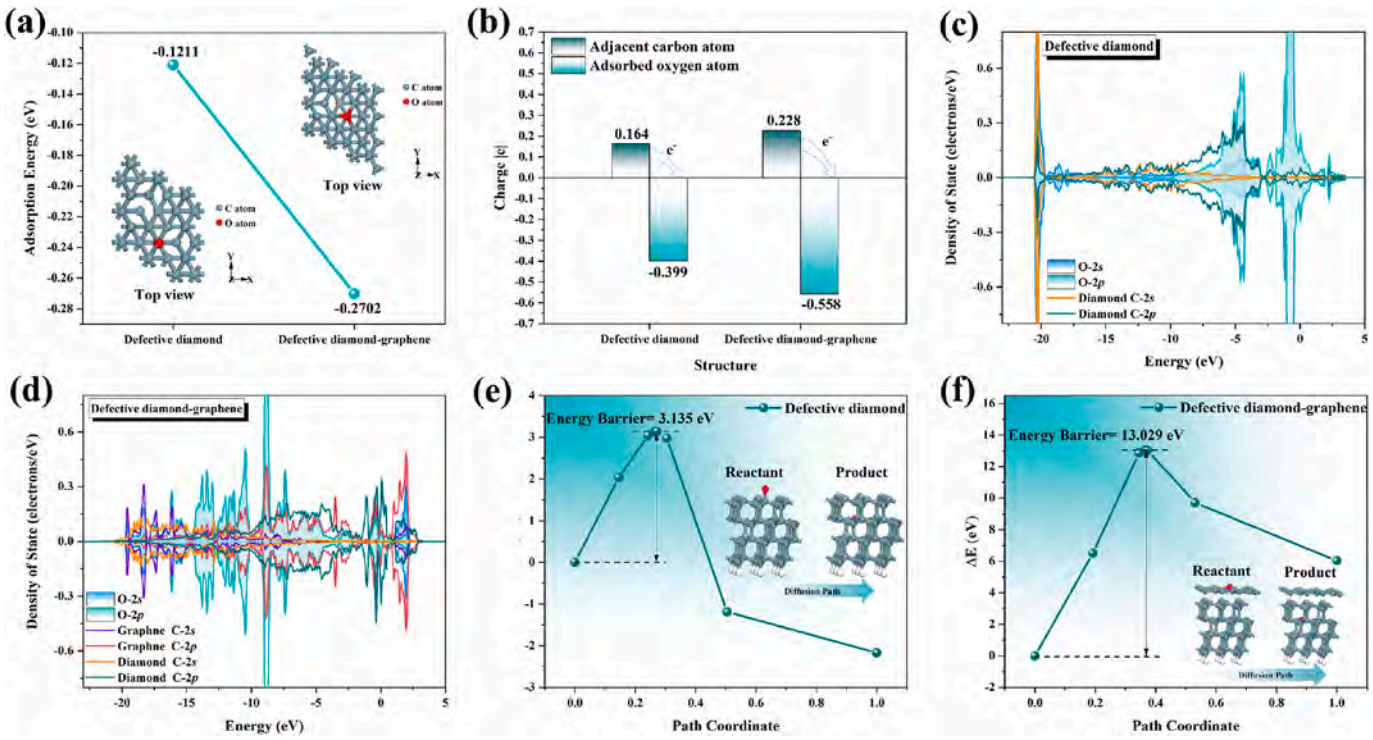


The authors would like to apologise for any inconvenience caused.

# Supplementary Material

# High-Temperature Friction and Oxidation Resistance of Self-Sacrificial Diamond-Graphene Heterostructures Coatings

Shuyu Fan[1,2], Shu Xiao[1*], Hu Zhang[1], Songsheng Lin[2*], Jing Wu[1], Fenghua Su[1], Paul K. Chu[3]

[1] School of Mechanical & Automotive Engineering, South China University of Technology, Guangzhou 510641, China

[2] Guangdong-Hong Kong Joint Laboratory of Modern Surface Engineering Technology, Guangdong Provincial Key Laboratory of Modern Surface Engineering Technology, Institute of New Materials, Guangdong Academy of Sciences, Guangzhou 510651, China

[3] Department of Physics, Department of Materials Science and Engineering, and Department of Biomedical Engineering, City University of Hong Kong, Tat Chee Avenue, Kowloon, Hong Kong, China

[*] Corresponding authors: xiaos@scut.edu.cn (S. Xiao); linsongsheng@gdinm.com (S.S. Lin)

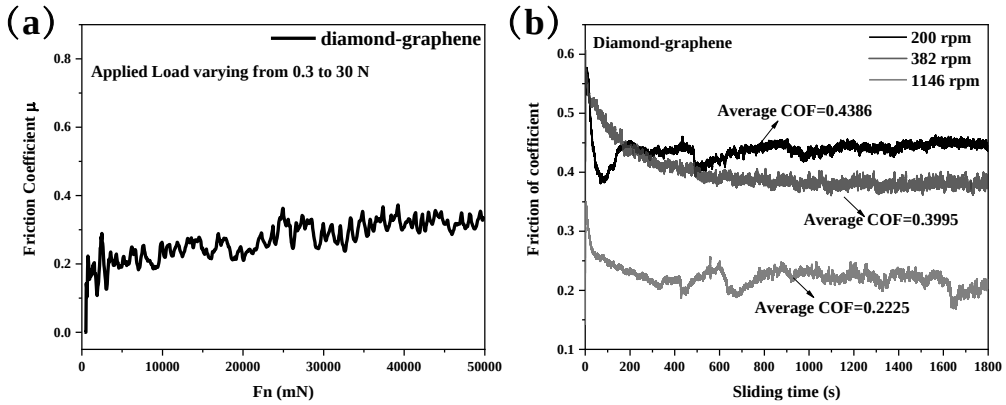


Fig. S1 Tribological properties of the diamond-graphene heterostructure coating under varying loads and rotation speeds: (a) Scratch test curves showing the evolution of friction coefficient (μ) with increasing normal load (Fn), demonstrating stable friction coefficient with minimal variation across the load range; (b) and corresponding average values measured at different rotation speeds (200, 382, and 1146 rpm), revealing a consistent decrease in friction coefficient with increasing rotation speed.

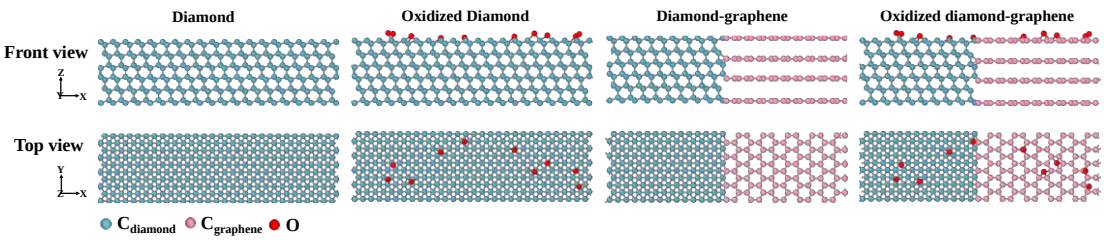


Fig. S2. Structural configurations showing front and top views of the diamond, oxidized diamond, diamond-graphene, and oxidized diamond-graphene structures.

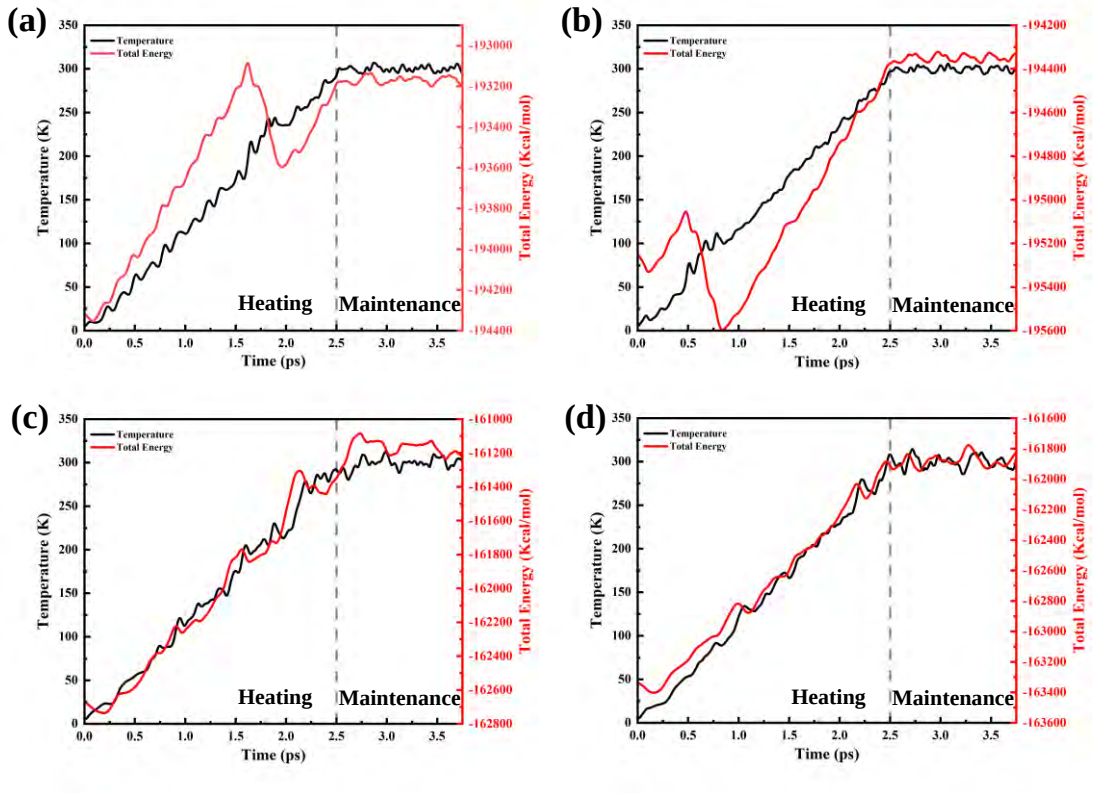


Fig. S3. Time evolution curves of temperature and total energy during both the heating and temperature maintenance stages in (a) diamond, (b)oxidized diamond, (c) diamond-graphene, and (d) oxidized diamond-graphene structures.

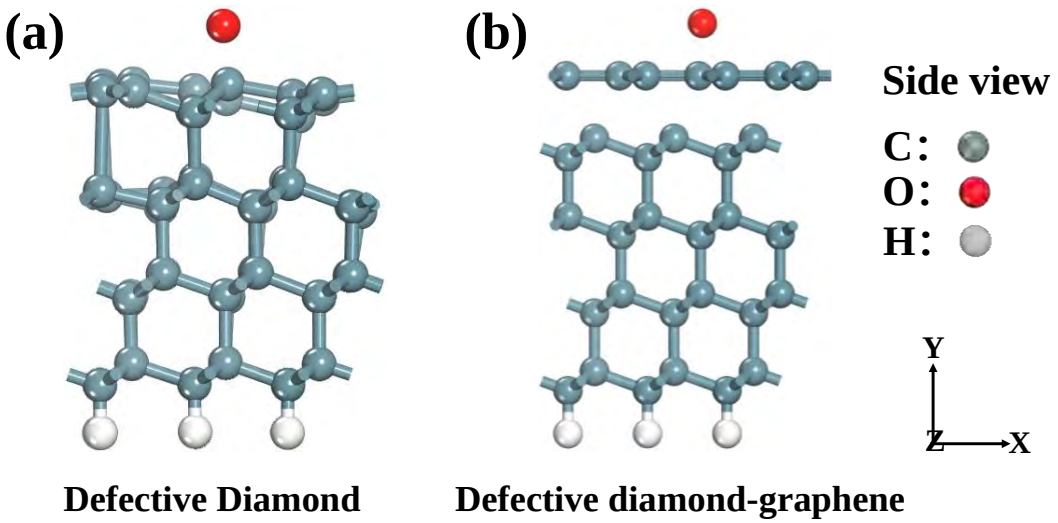


Fig. S4. Structural configurations showing side views of (a) defective diamond and (b) oxidized diamond-graphene structures with adsorbed oxygen atom.